

High-level, high-resolution ocean modeling at all scales with Oceananigans

Gregory L. Wagner¹, Simone Silvestri¹, Navid C. Constantinou^{2,3},
Ali Ramadhan⁴, Jean-Michel Campin¹, Chris Hill¹, Tomás Chor⁵,
Jago Strong-Wright⁶, Xin Kai Lee¹, Francis Poulin⁷, Andre Souza¹,
Keaton J. Burns^{1,8}, John Marshall¹, and Raffaele Ferrari¹

¹Massachusetts Institute of Technology, Cambridge, MA, USA

²University of Melbourne, Parkville, VIC, Australia

³ARC Center of Excellence for the Weather of the 21st Century, Australia

⁴atdepth MRV, Cambridge, MA, USA

⁵University of Maryland, College Park, MD, USA

⁶University of Cambridge, Cambridge, United Kingdom

⁷University of Waterloo, Waterloo, ON, Canada

⁸Flatiron Institute, New York, NY, USA

Key Points:

- Oceananigans provides a powerful interface for simulating oceanic motion at all scales with novel parameterizations and numerical methods.
- Combining simple numerics with GPU-enabled high-resolution permits accurate simulations with accessible code.
- High-level programmable interfaces are crucial to maximize both user and developer productivity.

22 **Abstract**

23 We describe the vision, user interface, governing equations, and numerical methods
 24 that underpin new ocean modeling software called “Oceananigans”. Oceananigans is being
 25 developed by the Climate Modeling Alliance as part of a larger project to build a trainable
 26 climate model with quantifiable uncertainty. We argue that Oceananigans status as a popular,
 27 capable modeling system realizes a vision for accelerating progress in Earth system modeling
 28 that balances demands for model accuracy and performance, needed for state-of-the-art
 29 science, against accessibility, which is needed to accelerate development. This vision combines
 30 three cooperative elements: *(i)* a relatively simple finite volume algorithm *(ii)* optimized for
 31 high-resolution simulations on GPUs which is *(iii)* exposed behind an expressive, high-level
 32 user interface (using the Julia programming language in our case). We offer evidence for
 33 the vision’s potential by illustrating the creative potential of our user interface, showcasing
 34 Oceananigans physics with example simulations that range from simple classroom problems to
 35 a realistic global ocean simulation spanning all scales of oceanic fluid motion, and describing
 36 advances in parameterization, numerical methods, and computational efficiency.

37 **Plain Language Summary**

38 This paper introduces Oceananigans, a new software tool for simulating ocean currents
 39 and fluid motion. Unlike most existing software for ocean modeling, Oceananigans is written
 40 in Julia, a modern programming language that makes it easier to install, learn, and use.
 41 Rather than relying on rigid configuration files, users write scripts, giving them more flexibility
 42 and creative control over their simulations. Moreover, Oceananigans can simulate everything
 43 from tiny millimeter-scale turbulence in a small box to planetary-scale ocean circulation.
 44 It is also fast and efficient, taking advantage of graphics processing units (GPUs) to run
 45 high-resolution simulations at speeds comparable to lower-resolution models in other software.
 46 Our goal is not just to provide a tool for scientists. Our approach to combine simple numerics
 47 on GPUs with a powerful user interface can accelerate the pace of model development, and
 48 therefore accelerate the pace of scientific progress.

49 **1 Introduction**

50 Computation is fundamental to ocean and climate science, such that software is rate-
 51 limiting for scientific progress. Since the first general circulation models ran on primitive
 52 computers (Phillips, 1956; Bryan, 1969), advances in hardware, numerical methods, and the
 53 approximate parameterization of otherwise unresolved processes have improved the fidelity
 54 of ocean simulations (Griffies et al., 2015). Yet as technology advances, the gap between
 55 potential and practice in ocean modeling is stagnant or widening, to the point that most
 56 software today *(i)* can no longer use the world’s fastest computers, *(ii)* relies on outdated
 57 user interfaces, and *(iii)* is still useful for only a limited subset of the wide variety of ocean
 58 modeling problems.

59 This paper describes new ocean modeling software written in the Julia programming
 60 language (Bezanson et al., 2017) called Oceananigans. Oceananigans is being developed
 61 by the Climate Modeling Alliance (along with heroic external collaborators) as part of
 62 a larger effort to develop a climate model automatically-calibrated to observations and
 63 high resolution simulations, and with quantified uncertainty. Oceananigans development
 64 is motivated primarily by the need for new capabilities. The most materially pressing
 65 is the need to implement a hierarchical approach to climate model development (Held,
 66 2005), wherein nonhydrostatic large eddy simulations are used to generate synthetic data
 67 for calibrating parameterizations, followed by the refinement of parameters in a hydrostatic
 68 global context against observations. Starting from scratch also allowed us to target GPUs
 69 and CPUs and to lower the bar for future accelerator support, by leveraging the performance
 70 portability offered by Julia’s KernelAbstractions (Churavy, 2024). Using GPUs reduces

71 the computational expense of ensemble calibration, enables higher resolution simulations,
 72 supports the next-generation of AI-based parameterizations, and makes ocean modeling
 73 cheaper and more accessible. Finally, and perhaps most important, we required a tool that
 74 was easy to use — not only for conducting creative science, but for quickly prototyping new
 75 parameterizations (Wagner, Hillier, et al., 2025), new numerical methods (Silvestri, Wagner,
 76 Campin, et al., 2024), and new algorithms for scaling simulations up to hundreds of GPUs
 77 (Silvestri, Wagner, Constantinou, et al., 2024). Our ultimate goal is to accelerate the *process*
 78 of model development and therefore, through a longer process of collective effort, accelerate
 79 progress in ocean and climate science.

80 1.1 From millimeters to millennia

81 The evolution of ocean circulation over millennia is controlled by turbulent mixing with
 82 scales that range down to millimeters. Two distinct systems have evolved to model and
 83 understand this huge range of oceanic motion: “GCMs” (general circulation models) for
 84 hydrostatic regional-to-global scale simulations, and simpler software for nonhydrostatic
 85 large eddy simulations (LESs) with meter-scale resolution that are high-fidelity but limited
 86 in duration and extent. Compared to LES, GCMs usually invoke more elaborate numerical
 87 methods and parameterizations to cope with the global ocean’s complex geometry and the
 88 more significant impacts of unresolved subgrid processes.

89 Oceananigans began as software for LES (Ramadhan et al., 2020), by perfecting an
 90 approach for hybrid hydrostatic/nonhydrostatic dynamical cores pioneered by MITgcm
 91 (Marshall, Adcroft, et al., 1997) for GPUs. Our nonhydrostatic LES algorithm was then
 92 adapted and optimized for a hydrostatic GCM (Silvestri, Wagner, Constantinou, et al., 2024).
 93 At the same time, we developed LES-inspired, minimally-dissipative numerical methods for
 94 turbulence-resolving simulations (Silvestri, Wagner, Campin, et al., 2024) that automatically
 95 adapt to changing resolution. The result is a computationally efficient modeling system
 96 suited to brute force, resolution-forced approach to accuracy for all scales of oceanic motion.
 97 Such a “LES the ocean” strategy is appealingly simple compared to alternatives relying
 98 on explicit dissipation, generalized vertical coordinates (Shchepetkin & McWilliams, 2005;
 99 Leclair & Madec, 2011; Petersen et al., 2015), Lagrangian vertical advection (Halliwell, 2004;
 100 Griffies et al., 2020), or unstructured horizontal grids (Ringler et al., 2013; Danilov et al.,
 101 2017; Korn et al., 2022). We hypothesize that “resolution everywhere” alleviates the need for
 102 unstructured targeted resolution and will reduce the spurious numerical mixing that pollutes
 103 the fidelity of lower-resolution simulations (Griffies et al., 2000), while yielding a plethora
 104 of additional improvements (Chassignet & Xu, 2017, 2021; Kiss et al., 2020). At the same
 105 time, using simple algorithms preserves the accessibility of our source code and maximizes
 106 the benefits of the Julia programming language.

107 1.2 Why programmable interfaces matter

108 In 1984, Cox published the first description of generalizable ocean modeling software
 109 (Cox, 1984; Griffies et al., 2015). The “Cox model” is written in FORTRAN 77 and features
 110 a multi-step user interface for building new models: first, source code modifications are
 111 written to determine, for example, domain geometry and boundary conditions, emplaced
 112 into the “base code”, and compiled. Next, a text-based namelist file is used to determine
 113 parameters like the stop iteration, mixing coefficients, and solver convergence criteria. Cox
 114 (1984) provided three example model configurations to illustrate the user interface.

115 With forty years of progress in software engineering, numerical methods, and parame-
 116 terization of unresolved processes, and more than a billion times more computational power,
 117 today’s ocean models bear little resemblance to the Cox model — *except* for their user inter-
 118 faces. Current interfaces, though obviously more advanced than Cox’s, still impose multi-step
 119 workflows that invoke several programming paradigms. These multi-step workflows typically
 120 require the generation of input data using a separate scripting language, configuration of

121 numerous namelists, and source code modifications to change the model equations in ways
122 not accessible through a change of parameters.

123 One of our most important contributions is the development of a fundamentally different,
124 programmable user interface that provides a seamless workflow for numerical experiments
125 including setup, execution, analysis, and visualization using a single script. Programmable
126 interfaces written in scripting languages like Python and Julia are the interface of choice
127 and engine of progress in countless fields from visualization to machine learning, and their
128 benefits transfer to ocean modeling. A particularly inspiring example of a productive user
129 interface for computational fluid dynamics is provided by Dedalus (Burns et al., 2020), a
130 CPU-based spectral framework for solving partial differential equations in simple geometries.

131 A programmable interface shines for simple problems — but doesn’t just help new users.
132 More importantly, this workflow accelerates the implementation of new numerical methods
133 and parameterizations by experienced developers. It facilitates writing and relentlessly
134 refactoring comprehensive test suites. It enables fast prototyping with tight implementation-
135 evaluation iterations. It makes it easier to collaborate by communicating concise but evocative
136 code snippets. It makes Oceananigans fun to use. Leveraging this programmable interface
137 together with the intrinsic productivity of the Julia programming language, Oceananigans
138 has progressed from a simple system for serial nonhydrostatic modeling (Ramadhan et
139 al., 2020) to parallelized software with capabilities at all scales up to global hydrostatic
140 simulations with breakthrough performance (Silvestri, Wagner, Constantinou, et al., 2024),
141 using innovative numerical methods (Silvestri, Wagner, Campin, et al., 2024) and new,
142 automatically-calibrated vertical mixing parameterizations (Wagner, Hillier, et al., 2025).
143 Users benefit too.

144 The Julia programming language, which is compiled and productive, has a lot to do
145 with the feasibility of our design. Unlike functions in pure Python, for example, Julia
146 functions implemented by users for forcing and boundary conditions can operate even in
147 high performance contexts on GPUs. Julia enables unique Oceananigans features, such as
148 interactivity, extensibility, automatic installation on any system, and portability to laptops
149 and GPUs through advanced Julia community tools (Besard et al., 2018; Churavy, 2024).
150 Oceananigans achieves breakthrough performance by using GPUs, but remains accessible to
151 students using personal laptops running Windows or Mac OS. Easy installation on personal
152 computers facilitates creative computation, since complex numerical experiments can be
153 prototyped productively in a comfortable personal environment before transferred to a high
154 performance environment for production runs.

155 Productive interfaces are only as powerful as the capability they expose. Oceananigans
156 combines a range of capabilities offered by other systems: a numerical design for modeling
157 across scales from MITgcm (Marshall, Adcroft, et al., 1997; Marshall, Hill, et al., 1997), a
158 simple and performant algorithm for LES from PALM and PyCLES (Pressel et al., 2015),
159 and GPU capabilities like Veros (Häfner et al., 2021), and scripting like Thetis (Kärnä et al.,
160 2018). Oceananigans assembles these diverse features behind an expressive programmable
161 interface.

162 1.3 Outline of this paper

163 This paper introduces the concepts that underpin Oceananigans’ user interface and
164 illustrates how a productive user interface can be designed to harness wide-ranging capabilities
165 for high-resolution modeling of any scale of oceanic motion. Our aim is to evidence and
166 explain Oceananigans tripartite achievement: performance, flexibility, and friendliness at the
167 same time. We do not attempt to document the specifics of the user interface in detail or to
168 provide a comprehensive description of all features, however: for that we refer the reader to
169 Oceananigans documentation.

170 Section 2 begins by explicating the basic innovations of Oceananigans’ programmable
 171 interface using two classroom examples: two-dimensional turbulence, and a forced passive
 172 tracer advected by two-dimensional turbulence. In section 3, we write down the governing
 173 equations that underpin Oceananigans’ nonhydrostatic and hydrostatic models. We build our
 174 case for Oceananigans innovations by progressing from simple direct numerical simulations
 175 of freshwater cabbeling and flow around a cylinder, to realistic tidally-forced large eddy
 176 simulations over a headland, to a 1/12th degree eddying global ocean simulation.

177 Section 4 provides a primer to the finite volume spatial discretization that Oceanani-
 178 gans uses to solve the nonhydrostatic and hydrostatic equations. This section establishes
 179 Oceananigans’ unique suitability for turbulence-resolving simulations that have minimal,
 180 implicitly dissipative advection schemes based on Weighted Essentially Non-Oscillatory
 181 (WENO) reconstruction. We conclude in section 6 by outlining future development work and
 182 anticipating the next major innovations in ocean modeling which, we hope, will someday
 183 render the present work obsolete.

184 2 Oceananigans, the library

185 Oceananigans is fundamentally a *library* of tools for building models by writing programs
 186 called “scripts”. This departs from the usual framework wherein software provides pre-written
 187 monolithic programs that are configured with parameters. For writing scripts, Oceananigans
 188 syntax combines mathematical symbols with natural language. Our goal is to enable evocative
 189 scripting that approaches the effectiveness of writing for communicating computational
 190 science.

191 2.1 Hello, ocean

192 The way to learn new ocean modeling software is by building simulations with it. Our
 193 first example in listing 1 sets up, runs, and visualizes a simulation of two-dimensional
 194 turbulence. The 22 lines of listing 1 illustrate one of Oceananigans’ main achievements: a
 195 numerical experiment may be completely described by a single script. To execute the code in
 196 listing 1, we need to copy into a file (call this, for example, `hello_ocean.jl`) and executed
 197 by typing `julia hello_ocean.jl` at a terminal.

198 Oceananigans scripts organize into four sections. The first three define the “grid” “model”,
 199 and “simulation”, and conclude with execution of the simulation. The fourth section, often
 200 implemented separately for complex or expensive simulations, performs post-processing and
 201 analysis. In listing 1, the grid defined on lines 4–7 determines the problem geometry, spatial
 202 resolution, and machine architecture. To use a CPU instead of a GPU, one writes `CPU()`
 203 in place of `GPU()` on line 5: no other changes to the script are required.

204 Lines 9–12 define the model, which solves the Navier–Stokes equations in two dimensions
 205 with a 9th-order Weighted, Essentially Non-Oscillatory (WENO) advection scheme (see
 206 section 4 for more information about WENO). The velocity components u, v are initialized
 207 with uniformly distributed random numbers within $[-1, 1)$. The model definition can also
 208 encompass forcing, boundary conditions, and the specification of additional terms in the
 209 momentum and tracer equations such as Coriolis forces or turbulence closures.

210 Line 14 builds a `Simulation` with a time-step $\Delta t = 0.01$ which will run until $t = 10$
 211 (Oceananigans does not assume dimensionality by default, so time is non-dimensional via
 212 user input in this case). `Simulation` can be used to inject arbitrary user code into the
 213 time-stepping loop in order to log simulation progress or write output to disk. Lines 17–19
 214 analyze the final state of the simulation by computing vorticity, illustrating Oceananigans’
 215 toolbox for building expression trees of discrete calculus and arithmetic operations. The same
 216 tools may be used to define online diagnostics to be periodically computed and saved to disk
 217 while the simulation runs. Line 22 concludes the numerical experiment with a visualization.
 218 The result is shown in figure 1.

```

1 using Oceananigans
2
3 # The third dimension is "flattened" to reduce the domain from three to two dimensions.
4 topology = (Periodic, Periodic, Flat)
5 architecture = GPU() # CPU() works just fine too for this small example.
6 x = y = (0, 2π)
7 grid = RectilinearGrid(architecture; size=(256, 256), x, y, topology)
8
9 model = NonhydrostaticModel(; grid, advection=WENO(order=9))
10
11 ε(x, y) = 2rand() - 1 # Uniformly-distributed random numbers between [-1, 1].
12 set!(model, u=ε, v=ε)
13
14 simulation = Simulation(model; Δt=0.01, stop_time=10)
15 run!(simulation)
16
17 u, v, w = model.velocities
18 ζ = ∂x(v) - ∂y(u)
19
20 using CairoMakie
21 heatmap(ζ, colormap=:balance, axis=(; aspect=1))

```

Listing 1: A Julia script that uses Oceananigans and the Julia plotting library CairoMakie to set up, run, and visualize a simulation of two-dimensional turbulence on a Graphics Processing Unit (GPU). The initial velocity field, defined on lines 11-12, consists of random numbers uniformly-distributed between -1 and 1 . The vorticity $\zeta = \partial_x v - \partial_y u$ is defined on line 18. The solution is visualized in figure 1.

```

1 function circling_source(x, y, t)
2     δ, ω, r = 0.1, 2π/3, 2
3     dx = x + r * cos(ω * t)
4     dy = y + r * sin(ω * t)
5     return exp(-(dx^2 + dy^2) / 2δ^2)
6 end
7
8 forcing = (; c = circling_source)
9 model = NonhydrostaticModel(; grid, advection=WENO(order=9), tracers=:c, forcing)

```

Listing 2: Implementation of a moving source of passive tracer with a function in a two-dimensional turbulence simulation. These lines of code replace the model definition on line 9 in listing 1.

219 2.2 Incorporating user code

220 With a programmable interface and aided by Julia’s just-in-time compilation, user
 221 functions specifying domain geometry, forcing, boundary conditions, and initial conditions
 222 can be incorporated directly into models without a separate programming environment. To
 223 illustrate function-based forcing, we modify listing 1 with code that adds a passive tracer
 224 which is forced by a moving source that that depends on x, y, t . A visualization of the
 225 vorticity and tracer field generated by listings 1 and 2 are shown in figure 1.

226 Users can also insert arbitrary functions for more general tasks into the time-stepping
 227 loop. This supports things as mundane as printing a summary of the current model status
 228 or writing output, to more exotic tasks like nudging state variables or updating a diffusion
 229 coefficient based on an externally-implemented model.

230 2.3 Abstractions for arithmetic and discrete calculus

231 Abstractions representing unary, binary, and calculus operators produce a system for
 232 building “lazy” expression trees, whose evaluation is delayed until their result is needed to be

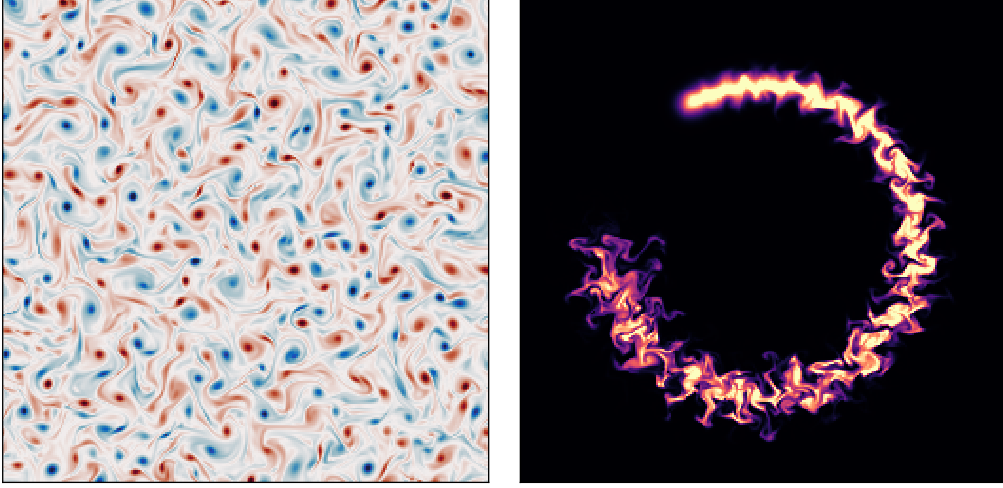


Figure 1: Vorticity after $t = 10$ (left) and a passive tracer injected by a moving source at $t = 2.5$ (right) in a simulation of two-dimensional turbulence using an implicitly-dissipative advection scheme.

233 saved to disk during a simulation. Example calculations representing vorticity, $\zeta = \partial_x v - \partial_y u$,
 234 speed $s = \sqrt{u^2 + v^2}$, and the x -integral of enstrophy $Z = \int_0^{2\pi} \zeta^2 dx$ are shown in listing 3.

```

236 1 u, v, w = model.velocities
237 2
238 3 # Lazy expression trees and reductions representing computations:
239 4  $\zeta = \partial_x(v) - \partial_y(u)$ 
240 5  $s = \sqrt{u^2 + v^2}$ 
241 6  $Z = \text{Integral}(\zeta^2, \text{dims}=1)$ 
242
244
```

Listing 3: “Lazy” abstractions for expression trees and reductions — abstractions that *represent* computations to be performed at some future time as needed — support custom online diagnostics.

245 3 Governing equations and physical parameterizations

246 Oceananigans implements two “models” for ocean-flavored fluid dynamics: the Hydrostat-
 247 icFreeSurfaceModel, and the NonhydrostaticModel. Each represents a template for equations
 248 that govern the evolution of momentum and tracers. Both models are incompressible and
 249 make the Boussinesq approximation, which means that the density of the modeled fluid is
 250 decomposed into a constant reference ρ_0 and a small dynamic perturbation ρ' ,

$$\rho(\mathbf{x}, t) = \rho_0 + \rho'(\mathbf{x}, t) \quad \text{where} \quad \rho' \ll \rho_0, \quad (1)$$

251 and $\mathbf{x} = (x, y, z)$ is position and t is time.

252 The relative smallness of ρ' reduces conservation of mass to a statement of incompress-
 253 ibility called the continuity equation,

$$\nabla \cdot \mathbf{u} = 0, \quad (2)$$

254 where

$$\mathbf{u} \stackrel{\text{def}}{=} u \hat{\mathbf{x}} + v \hat{\mathbf{y}} + w \hat{\mathbf{z}}, \quad (3)$$

255 is the three-dimensional velocity field. Within the Boussinesq approximation, the momentum
 256 $\rho_0 \mathbf{u}$ varies only with the velocity \mathbf{u} . The effect of density variations is encapsulated by a

257 buoyant acceleration,

$$b \stackrel{\text{def}}{=} -\frac{g\rho'}{\rho_0}, \quad (4)$$

258 where g is gravitational acceleration. The “buoyancy” b acts in the direction of gravity.

259 The total dynamic pressure P is decomposed into

$$P = \rho_0 g z + \rho_0 p(\mathbf{x}, t), \quad (5)$$

260 where $\rho_0 g z$ is the static contribution to pressure that opposes the gravitational force associated
 261 with the reference density ρ_0 , and $\rho_0 p$ represents the dynamic anomaly. p is called the
 262 kinematic pressure.

263 3.1 The NonhydrostaticModel

264 The NonhydrostaticModel represents the Boussinesq equations formulated *without*
 265 making the hydrostatic approximation typical to general circulation models. The Nonhydro-
 266 staticModel has a three-dimensional prognostic velocity field.

267 3.1.1 The NonhydrostaticModel momentum equation

268 The NonhydrostaticModel’s momentum equation incorporates advection by a background
 269 velocity field, Coriolis forces, surface wave effects via the Craik-Leibovich asymptotic model
 270 (Craik & Leibovich, 1976; Huang, 1979), a buoyancy term allowed to be a nonlinear function
 271 of tracers and depth, a stress divergence derived from molecular friction or a turbulence
 272 closure, and a user-defined forcing term. Using the Boussinesq approximation in (1) and
 273 the pressure decomposition in (5), the generic form of NonhydrostaticModel’s momentum
 274 equation is

$$\begin{aligned} \partial_t \mathbf{u} = & -\nabla p - \underbrace{(\mathbf{u} \cdot \nabla) \mathbf{u} - (\mathbf{u}_g \cdot \nabla) \mathbf{u} - (\mathbf{u} \cdot \nabla) \mathbf{u}_g}_{\text{advection}} - \underbrace{\mathbf{f} \times \mathbf{u}}_{\text{Coriolis}} \\ & + \underbrace{(\nabla \times \mathbf{u}_s) \times \mathbf{u} + \partial_t \mathbf{u}_s}_{\text{Stokes drift}} - \underbrace{b \hat{\mathbf{g}}}_{\text{buoyancy}} - \underbrace{\nabla \cdot \boldsymbol{\tau}}_{\text{closure}} + \underbrace{\mathbf{F}_u}_{\text{forcing}}, \end{aligned} \quad (6)$$

275 where \mathbf{u}_g is a prescribed “background” velocity field, p is the kinematic pressure, \mathbf{f} is the
 276 background vorticity associated with a rotating frame of reference, \mathbf{u}_s is the Stokes drift
 277 profile associated with a prescribed surface wave field, b is buoyancy, $\hat{\mathbf{g}}$ is the gravitational
 278 unit vector (usually pointing downwards, that is, $\hat{\mathbf{g}} = -\hat{\mathbf{z}}$), $\boldsymbol{\tau}$ is the stress tensor associated
 279 with molecular viscous or subgrid turbulent momentum transport, and \mathbf{F}_u is a body force.

280 To integrate equation (6) while enforcing (2), we use a pressure correction method
 281 that requires solving a three-dimensional Poisson equation to find p , which can be derived
 282 from $\nabla \cdot (6)$. This Poisson equation is often a computational bottleneck in curvilinear or
 283 irregular domains, and its elimination is the main motivation for making the hydrostatic
 284 approximation when formulating the HydrostaticFreeSurfaceModel, as described in section 3.2.
 285 For rectilinear grids, we solve the Poisson equation using a fast, direct, mixed FFT-tridiagonal
 286 solver (Schumann & Sweet, 1988), providing substantial acceleration over MITgcm’s conjugate
 287 gradient pressure solver (Marshall, Adcroft, et al., 1997). In irregular domains, we either use a
 288 masking method that permits an approximate solution of the pressure Poisson equation with
 289 the FFT-based method, or a rapidly-converging conjugate gradient iteration that leverages
 290 the FFT-based solver as a preconditioner. The pressure correction scheme is described
 291 further in appendix A2.

292 Using (2), advection in the NonhydrostaticModel is formulated in the “flux form”, which
 293 is conveniently expressed with indicial notation,

$$\text{advection} = u_j \partial_j u_i + u_{g_j} \partial_j u_i + u_j \partial_j u_{g_i} = \partial_j \left[(u_j + u_{g_j}) u_i + u_j u_{g_i} \right], \quad (7)$$

294 where, for example, the i -th component of the advection term is $[(\mathbf{u} \cdot \nabla) \mathbf{u}]_i = u_j \partial_j u_i$.

295 The formulation of the Stokes drift terms means that \mathbf{u} is the Lagrangian-mean velocity
 296 when Stokes drift effects are included (see, for example, [Wagner et al., 2021](#)). With a
 297 Lagrangian-mean formulation, equations (2) and (6) are consistent only when \mathbf{u}_s is non-
 298 divergent — or equivalently, when \mathbf{u}_s is obtained by projecting the divergence out of the
 299 usual Stokes drift ([Vanneste & Young, 2022](#)). As discussed by [Wagner et al. \(2021\)](#), the
 300 Lagrangian-mean formulation of (6) means that closures for LES strictly destroy kinetic
 301 energy, avoiding the inconsistency between resolved and subgrid fluxes affecting typical LES
 302 formulated in terms of the Eulerian-mean velocity (see also [Pearson, 2018](#)).

303 The labeled terms in (6) are controlled by arguments to `NonhydrostaticModel` invoked
 304 in both of listings 1 and 2. For example, “advection” chooses a numerical scheme to
 305 approximate the advection term in (6) and (7). As another example, we consider configuring
 306 the closure term in (6) to represent (i) molecular diffusion by a constant-coefficient Laplacian
 307 `ScalarDiffusivity`, (ii) turbulent stresses approximated by the SmagorinskyLilly eddy viscosity
 308 model ([Smagorinsky, 1963](#); [Lilly, 1983](#)) for large eddy simulation, or (iii) omitting it entirely,
 309 which we use with WENO advection schemes (and which is also our default setting). In
 310 these three cases, the closure flux divergence $\nabla \cdot \boldsymbol{\tau} = \partial_m \tau_{nm}$ in indicial notation becomes

$$-\partial_m \tau_{nm} = \begin{cases} \partial_m (\nu \partial_m u_n) & \text{(ScalarDiffusivity)} \\ 0 & \text{(nothing)} \\ \partial_m \left(\underbrace{2 C_s \Delta^2 |\Sigma|}_{\nu_e} \Sigma_{nm} \right) & \text{(SmagorinskyLilly)} \end{cases} \quad (8)$$

311 where ν is the Laplacian diffusion coefficient, $\Sigma_{nm} = \partial_m u_n + \partial_n u_m$ is the strain rate tensor,
 312 $|\Sigma|$ is the magnitude of the strain rate tensor, C_s is the SmagorinskyLilly model constant,
 313 Δ scales with the local grid spacing, and ν_e is the eddy viscosity. (`ScalarDiffusivity` diffusion
 314 coefficients may also vary in time- and space. Other closure options include fourth-order
 315 `ScalarBiharmonicDiffusivity`, various flavors of `DynamicSmagorinsky` ([Bou-Zeid et al., 2005](#)),
 316 and the `AnisotropicMinimumDissipation` turbulence closure ([Rozema et al., 2015](#); [Vreugdenhil](#)
 317 [& Taylor, 2018](#)) for large eddy simulations.)

318 Listing 4 implements a direct numerical simulation of uniform flow past a cylinder
 319 with no-slip boundary conditions, a molecular `ScalarDiffusivity`, and a centered second-
 320 order advection scheme. Lines 6–7 embed a cylindrical mask in a `RectilinearGrid` using a
 321 `GridFittedBoundary`, which generalizes to arbitrary three-dimensional shapes. The no-slip
 322 condition is implemented with `ValueBoundaryCondition` (a synonym for “Dirichlet” boundary
 323 conditions) on lines 11–12. Other choices include `GradientBoundaryCondition` (Neumann),
 324 `FluxBoundaryCondition` (direct imposition of fluxes), and `OpenBoundaryCondition` (for
 325 non-trivial boundary-normal velocity fields).

326 Results obtained with listing 4 for $Re = 100$, $Re = 1000$, and a modified version of
 327 listing 4 for large eddy simulation ($Re \rightarrow \infty$) are visualized in figure 2. To adapt listing 4
 328 for LES, the closure is eliminated in favor of a 9th-order WENO advection scheme, and the
 329 no-slip boundary condition is replaced with a quadratic drag boundary condition with a drag
 330 coefficient estimated from similarity theory using a constant estimated roughness length.

331 3.1.2 The `NonhydrostaticModel` tracer conservation equation

332 The buoyancy term in (6) requires tracers, and can be formulated to use buoyancy
 333 itself as a tracer, or to depend on temperature T and salinity S . For seawater, a 54-
 334 term polynomial approximation `TEOS10EquationOfState` ([McDougall & Barker, 2011](#);
 335 [Roquet, Madec, McDougall, & Barker, 2015](#)) is implemented in the auxiliary package
 336 `SeawaterPolynomials`, along with quadratic approximations to TEOS-10 ([Roquet, Madec,](#)
 337 [Brodeau, & Nycander, 2015](#)) and a `LinearEquationOfState`. All tracers — either “active”

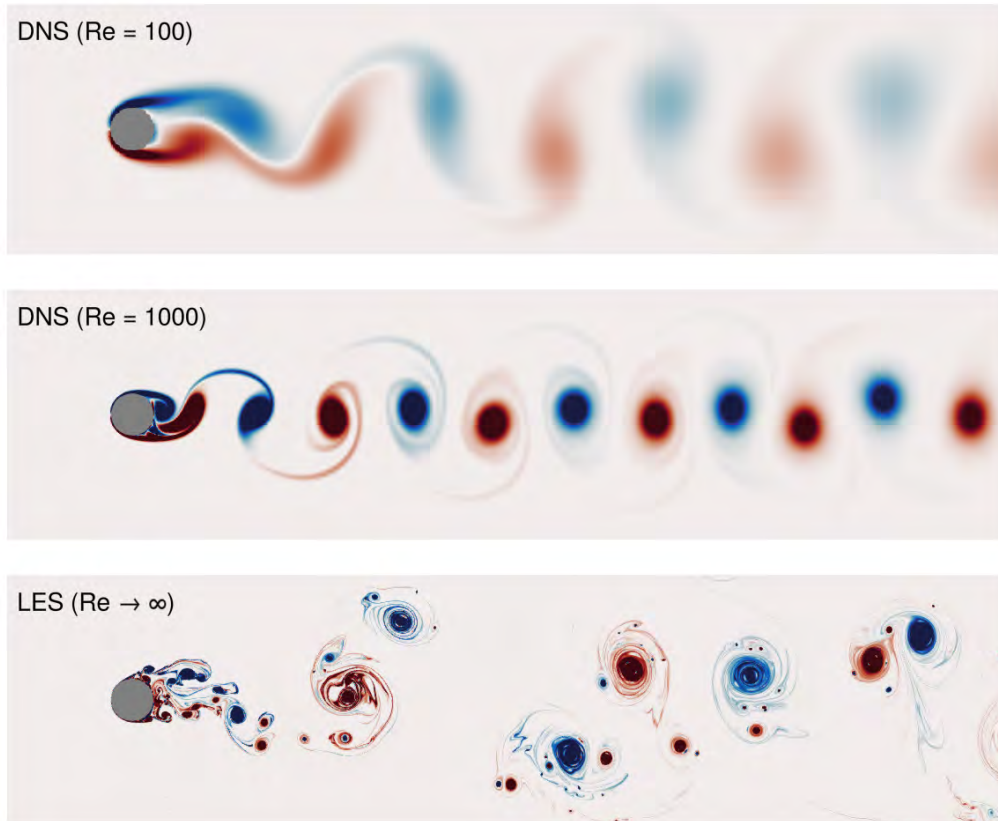


Figure 2: Vorticity snapshots in simulations of flow around a cylinder. The top two panels show vorticity in direct numerical simulations (DNS) that use a molecular ScalarDiffusivity closure and Centered(order=2) advection. The bottom panel shows a large eddy simulation (LES) with no closure and a WENO(order=9) advection scheme.

```

1 r, U, Re, Ny = 1/2, 1, 1000, 2048
2
3 grid = RectilinearGrid(GPU(), size=(2Ny, Ny), x=(-3, 21), y=(-6, 6),
4 topology=(Periodic, Bounded, Flat))
5
6 cylinder(x, y) = (x^2 + y^2) <= r^2
7 grid = ImmersedBoundaryGrid(grid, GridFittedBoundary(cylinder))
8
9 closure = ScalarDiffusivity(ν=1/Re)
10
11 no_slip = FieldBoundaryConditions(immersed=ValueBoundaryCondition(0))
12 boundary_conditions = (u=no_slip, v=no_slip)
13
14 # Implement a sponge layer on the right side of the domain that
15 # relaxes v → 0 and u → U over a region of thickness δ
16 @inline mask(x, y, δ=3, x0=21) = max(zero(x), (x - x0 + δ) / δ)
17 Fu = Relaxation(target=U; mask, rate=1)
18 Fv = Relaxation(target=0; mask, rate=1)
19
20 model = NonhydrostaticModel(; grid, closure, boundary_conditions, forcing=(u=Fu, v=Fv))

```

Listing 4: Direct numerical simulation of flow past a cylinder at various Reynolds numbers Re . The domain is periodic in x and a sponge layer on the right side of relaxes the solution to $\mathbf{u} = u_\infty \hat{\mathbf{x}}$ with $u_\infty = 1$. The experiment can be converted to a large eddy simulation (thereby sending $Re \rightarrow \infty$) by replacing the no-slip boundary conditions with an appropriate drag model and either (i) using an appropriate turbulence closure or (ii) using the WENO(order=9) advection scheme with no turbulence closure. Visualizations of the DNS and LES cases are shown in figure 2.

338 tracers required to compute the buoyancy term, as well as additional user-defined passive
339 tracers — obey the tracer conservation equation

$$\partial_t c = \underbrace{-(\mathbf{u} \cdot \nabla) c - (\mathbf{u}_g \cdot \nabla) c - (\mathbf{u} \cdot \nabla) c_g}_{\text{advection}} - \underbrace{\nabla \cdot \mathbf{J}_c}_{\text{closure}} + \underbrace{S_c}_{\text{biogeochemistry}} + \underbrace{F_c}_{\text{forcing}}, \quad (9)$$

340 where c represents any tracer, c_g represents a prescribed background tracer concentration
341 for c , \mathbf{J}_c is a tracer flux associated with molecular diffusion or subgrid turbulence, S_c is a
342 source or sink term associated with biogeochemical transformations (provided, for example,
343 by external packages like OceanBioME; Strong-Wright et al., 2023), and F_c is a user-defined
344 source or sink.

345 A simulation with a passive tracer having a user-defined source term is illustrated by
346 listing 2 and figure 1. For a second example, we consider freshwater cabbeling. Cabbeling
347 occurs when two water masses of similar density mix to form a new water mass which,
348 due to the nonlinearity of the equation of state, is denser than either of its constituents.
349 Freshwater, for example, is densest at 4 degrees Celsius, while 1- and 7.55-degree water are
350 lighter with roughly the same density. We implement a direct numerical simulation in which
351 7.55-degree water overlies 1-degree water, using the TEOS10EquationOfState provided by
352 the auxiliary package SeawaterPolynomials. The script is shown in listing 5. The resulting
353 density and temperature fields after 1 minute of simulation are shown in figure 3. Note that
354 the TEOS10EquationOfState typically depends on both temperature and salinity tracers,
355 but listing 5 specifies a constant salinity $S = 0$ and thus avoids allocating memory for or
356 simulating salinity directly.

```

357
358
359 1 grid = RectilinearGrid(GPU(), topology = (Bounded, Flat, Bounded),
360 size = (4096, 1024), x = (0, 2), z = (-0.5, 0))
361
362 2
363 3 closure = ScalarDiffusivity(ν=1.15e-6, κ=1e-7)
364
365 4
366 5
367 6 using SeawaterPolynomials: TEOS10EquationOfState
368 7 equation_of_state = TEOS10EquationOfState(reference_density=1000)

```

```

366 8
367 9 buoyancy = SeawaterBuoyancy(gravitational_acceleration = 9.81);
368 10 constant_salinity = 0, # set S=0 and simulate T only
369 11 equation_of_state)
370 12
371 13 model = NonhydrostaticModel(; grid, buoyancy, closure, tracers=:T)
372 14
373 15 Ti(x, z) = z > -0.25 ? 7.55 : 1
374 16 Ξi(x, z) = 1e-2 * randn()
375 17 set!(model, T=Ti, u=Ξi, v=Ξi, w=Ξi)
376

```

Listing 5: Direct numerical simulation of convective turbulence driven by cabelling between 1- and 7.55-degree freshwater. ν denotes viscosity and κ denotes the tracer diffusivity. The diffusivity may also be set independently for each tracer.

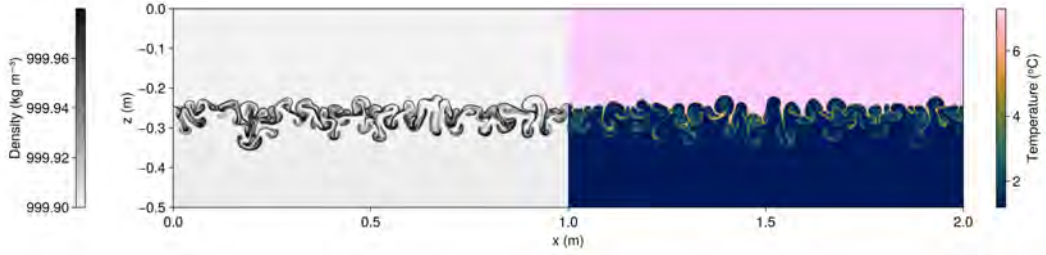


Figure 3: Density and temperature at $t = 1$ minute in a direct numerical simulation of cabelling in freshwater. Note that both fields span from $x = 0$ to $x = 2$ meters; only the left half of the density field and the right half of the temperature field are shown.

We next consider a large eddy simulation of the Eady problem (Eady, 1949). In the Eady problem, perturbations evolve around a basic state with constant shear Λ in thermal wind balance with a constant meridional buoyancy gradient $f\Lambda$, such that

$$u = \underbrace{\Lambda z}_{\text{def } U} + u', \quad \text{and} \quad b = \underbrace{-f\Lambda y}_{\text{def } B} + b'. \quad (10)$$

We use Oceananigans’ BackgroundFields to simulate the nonlinear evolution of (u', v, w) and b' expanded around U and B in a doubly-periodic domain. We impose an initially stable density stratification with $b' = N^2 z$ and $N^2 = 10^{-7} \text{ s}^{-2}$ superposed with random noise. The Richardson number of the initial condition is $Ri = N^2 / \partial_z U = N^2 / \Lambda$; we choose mean shear Λ so that $Ri = 1$, which guarantees the basic state is unstable to baroclinic instability but stable to symmetric and Kelvin-Helmholtz instability (Stone, 1971). A portion of the script is shown in listing 6.

Our Eady simulation uses fully-turbulence-resolving resolution with 4 meter horizontal spacing and 2 meter vertical spacing in a $4 \text{ km} \times 4 \text{ km} \times 128 \text{ m}$ domain and simulates 30 days on a single Nvidia H100 GPU. Four snapshots of vertical vorticity normalized by f (the Rossby number) are shown in figure 4, illustrating the growth of kilometer-scale vortex motions amid bursts of meter-scale three-dimensional turbulence that develop along thin filaments of vertical vorticity and vertical shear. This simple configuration captures a competition between baroclinic instability, which acts to “restratify” or strengthen boundary layer stratification, and three-dimensional turbulent mixing driven either by a forward cascade from kilometer-scale motions (Molemaker et al., 2010; Dong et al., 2024) or atmospheric storms (Boccaletti et al., 2007; Callies & Ferrari, 2018).

Finally, we illustrate Oceananigans’ capabilities for realistic, three-dimensional large eddy simulations in complex geometries by simulating temperature- and salinity-stratified

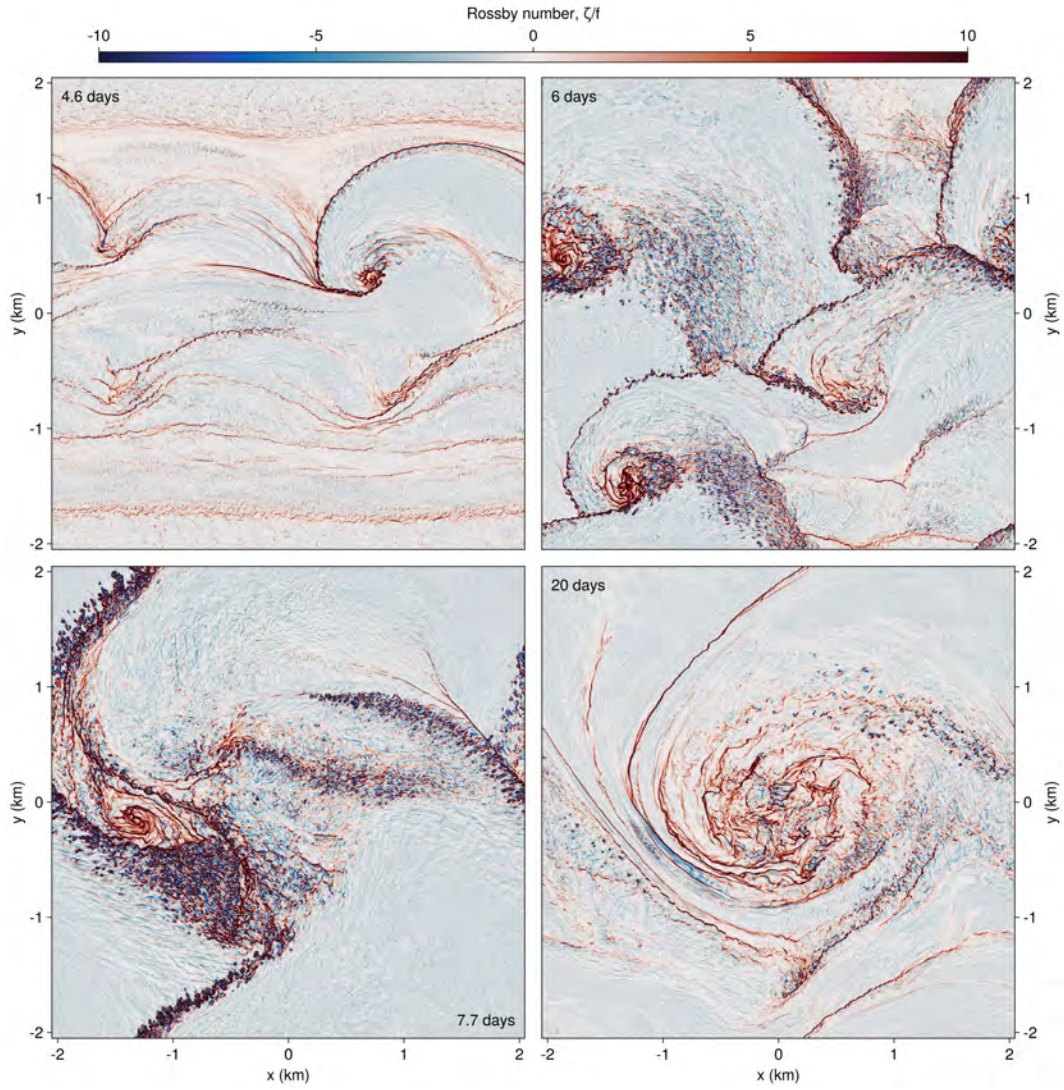


Figure 4: Surface vertical vorticity in a large eddy simulation of the Eady problem with $Ri = 1$ initially, after $t = 4.6, 6, 7.7,$ and 20 days. The grid spacing is $4 \times 4 \times 2$ meters in x, y, z . Part of the script that produces this simulation is show in listing 6.

```

1 grid = RectilinearGrid(GPU(); size = (1024, 1024, 64),
2                       x = (0, 4096), y = (0, 4096), z = (0, 128),
3                       topology=(Periodic, Periodic, Bounded))
4
5 f, N2, Ri = 1e-4, 1e-7, 1
6 parameters = (f=f, Λ=sqrt(N2/Ri)) # U = Λz, so Ri = N2 / ∂z(U) = N2 / Λ and Λ = N / √Ri.
7
8 @inline U(x, y, z, t, p) = + p.Λ * z
9 @inline B(x, y, z, t, p) = - p.f * p.Λ * y
10
11 background_fields = (u = BackgroundField(U; parameters),
12                     b = BackgroundField(B; parameters))
13
14 model = NonhydrostaticModel(; grid, background_fields,
15                             advection = WENO(order=9), coriolis = FPlane(; f),
16                             tracers = :b, buoyancy = BuoyancyTracer())
17
18 Δz = minimum_zspacing(grid)
19 bi(x, y, z) = N2 * z + 1e-2 * N2 * Δz * (2rand() - 1)
20 set!(model, b=bi)

```

Listing 6: Large eddy simulation of the Eady problem expanded around the background geostrophic shear with $Ri = 1$.

400 tidal flow past a headland, reminiscent of an extensively observed and modeled flow past
 401 Three Tree Point in Puget Sound in the Pacific Northwest of the United States (Pawlak et
 402 al., 2003; Warner & MacCready, 2014). The bathymetry involves a sloping wedge that juts
 403 from a square-sided channel, such that

$$z_b(x, y) = -H \left(1 + \frac{y + |x|}{\delta} \right), \quad (11)$$

404 where $\delta = L/2$ represents the scale of the bathymetry, L is the half-channel width in y (the
 405 total width is $2L$), and $H = 128$ m is the depth of the channel, and $z = z_b(x, y)$ is the height
 406 of the bottom. The flow is driven by a tidally-oscillating boundary velocity

$$U(t) = U_2 \sin \left(\frac{2\pi t}{T_2} \right) \quad (12)$$

407 imposed at the east and west boundaries. Here, $T_2 = 12.421$ hours is the period of the
 408 semi-diurnal lunar tide, and $U_2 = 0.15$ m s⁻¹ is the characteristic tidal velocity around Three
 409 Tree Point. The initial temperature and salinity are

$$T|_{t=0} = 12 + 4 \frac{z}{H} \text{ } ^\circ\text{C}, \quad \text{and} \quad S|_{t=0} = 32 \text{ g kg}^{-1}. \quad (13)$$

410 A portion of the script that implements this simulation is shown in listing 7.

411 The oscillatory, turbulent flow is visualized in figure 5. The calculation of Ertel Potential
 412 Vorticity shown in figure 5c uses the companion package Oceanostics (Chor et al., 2025).

413 3.2 Hydrostatic model with a free surface

414 The HydrostaticFreeSurfaceModel solves the *hydrostatic*, rotating Boussinesq equations
 415 with a free surface. The hydrostatic approximation, inherent to the HydrostaticFreeSurface-
 416 Model, means that the vertical momentum equation used by NonhydrostaticModel, $\hat{\mathbf{z}} \cdot (6)$,
 417 is replaced by a statement of hydrostatic balance,

$$\partial_z p = b, \quad (14)$$

418 while the vertical velocity is obtained diagnostically from the continuity equation,

$$\partial_z w = -\nabla_h \cdot \mathbf{u}_h. \quad (15)$$

```

1 H, L = 256meters, 1024meters
2  $\delta$  = L / 2
3 x, y, z = (-3L, 3L), (-L, L), (-H, 0)
4 Nz = 64
5
6 grid = RectilinearGrid(GPU(); size=(6Nz, 2Nz, Nz), halo=(6, 6, 6),
7     x, y, z, topology=(Bounded, Bounded, Bounded))
8
9 wedge(x, y) = -H * (1 + (y + abs(x)) /  $\delta$ )
10 grid = ImmersedBoundaryGrid(grid, GridFittedBottom(wedge))
11
12 T2 = 12.421hours
13 U2 = 0.1 # m/s
14
15 @inline Fu(x, y, z, t, p) = 2 $\pi$  * p.U2 / p.T2 * cos(2 $\pi$  * t / p.T2)
16 @inline U(x, y, z, t, p) = p.U2 * sin(2 $\pi$  * t / p.T2)
17 @inline U(y, z, t, p) = U(zero(y), y, z, t, p)
18
19 open_bc = PerturbationAdvectionOpenBoundaryCondition(U; inflow_timescale = 2minutes,
20     outflow_timescale = 2minutes,
21     parameters=(; U2, T2))
22
23 u_bcs = FieldBoundaryConditions(east = open_bc, west = open_bc)
24
25 @inline ambient_temperature(x, z, t, H) = 12 + 4z/H
26 @inline ambient_temperature(x, y, z, t, H) = ambient_temperature(x, z, t, H)
27 ambient_temperature_bc = ValueBoundaryCondition(ambient_temperature; parameters = H)
28 T_bcs = FieldBoundaryConditions(east = ambient_temperature_bc,
29     west = ambient_temperature_bc)
30
31 ambient_salinity_bc = ValueBoundaryCondition(32)
32 S_bcs = FieldBoundaryConditions(east = ambient_salinity_bc, west = ambient_salinity_bc)
33
34 buoyancy = SeawaterBuoyancy(equation_of_state=TEOS10EquationOfState())
35
36 model = NonhydrostaticModel(; grid, buoyancy,
37     tracers = (:T, :S),
38     advection = WENO(order=9),
39     coriolis = FPlane(latitude=47.5),
40     boundary_conditions = (; T=T_bcs, u = u_bcs, S = S_bcs))
41
42 Ti(x, y, z) = ambient_temperature(x, y, z, 0, H)
43
44 set!(model, T=Ti, S=32, u=U(0, 0, 0, 0, (; U2, T2)))

```

Listing 7: Large eddy simulation of flow past a headland reminiscent of Three Tree Point in the Pacific Northwest (see Pawlak et al., 2003; Warner & MacCready, 2014).

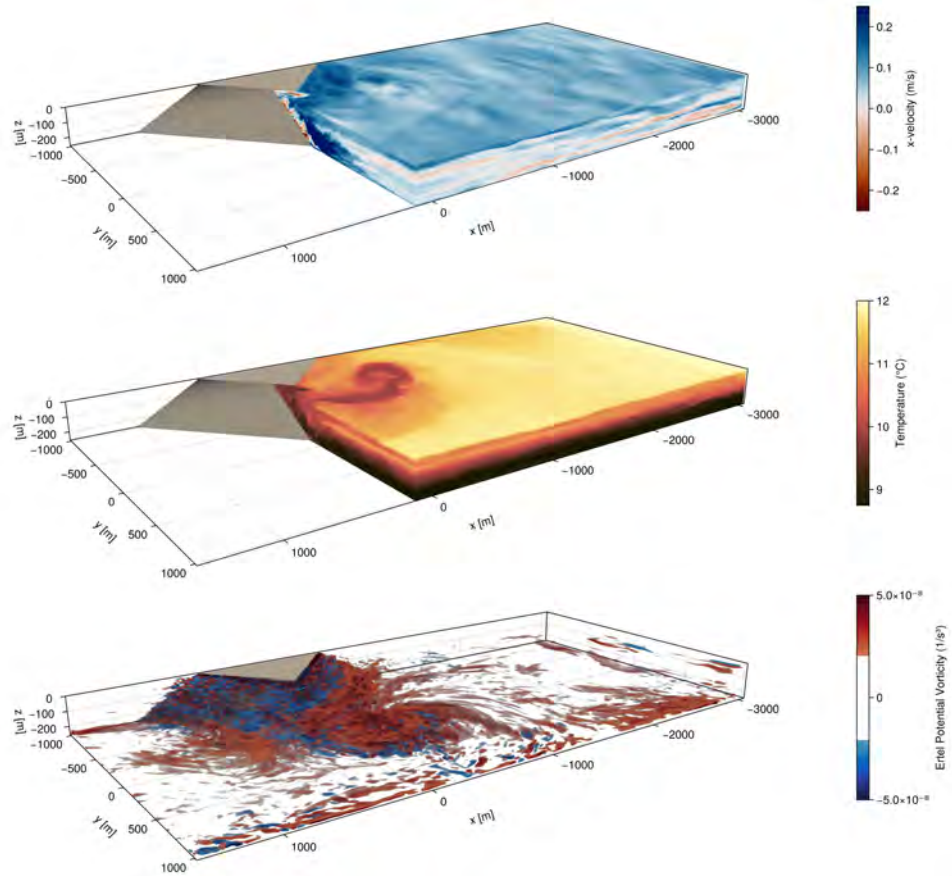


Figure 5: Along-channel velocity, temperature, and Ertel potential vorticity in a tidally-forced flow past an idealized headland with open boundaries. The tidal flow occurs in the x -directions and the snapshot depicts the flow just after the tide has turned to the negative- x direction.

419 As a result, time-stepping the HydrostaticFreeSurfaceModel does require solving a three-
 420 dimensional Poisson equation for pressure. Moreover, the HydrostaticFreeSurfaceModel
 421 introduces a free surface displacement η , which obeys the linearized equation

$$\partial_t \eta = w|_{z=0}. \quad (16)$$

422 Equation (16) replaces the rigid-lid impenetrability condition $w|_{z=0} = 0$ typically applied at
 423 top boundaries in the NonhydrostaticModel. The numerical algorithms and computational
 424 performance of the HydrostaticFreeSurfaceModel are described in more detail by [Silvestri,](#)
 425 [Wagner, Constantinou, et al. \(2024\)](#).

426 In the HydrostaticFreeSurfaceModel, the horizontal momentum $\mathbf{u}_h = u \hat{\mathbf{x}} + v \hat{\mathbf{y}}$ evolves
 427 according to

$$\partial_t \mathbf{u}_h = -\nabla_h p - \underbrace{g \nabla_h \eta}_{\text{free surface}} - \underbrace{(\mathbf{u} \cdot \nabla) \mathbf{u}_h}_{\text{momentum advection}} - \underbrace{\mathbf{f} \times \mathbf{u}}_{\text{Coriolis}} - \underbrace{\nabla \cdot \boldsymbol{\tau}}_{\text{closure}} + \underbrace{\mathbf{F}_{uh}}_{\text{forcing}}, \quad (17)$$

428 where p is the hydrostatic kinematic pressure anomaly, η is the free surface displacement,
 429 $\mathbf{u} = u \hat{\mathbf{x}} + v \hat{\mathbf{y}} + w \hat{\mathbf{z}}$ is the three-dimensional velocity, \mathbf{f} is the background vorticity associated
 430 with a rotating frame of reference, $\boldsymbol{\tau}$ is the stress associated with subgrid turbulent horizontal
 431 momentum transport, and \mathbf{F}_{uh} is a body force. Momentum advection can be formulated in
 432 three ways,

$$(\mathbf{u} \cdot \nabla) \cdot \mathbf{u}_h = \begin{cases} \nabla \cdot (\mathbf{u} \mathbf{u}_h) & \text{“flux form”,} \\ \zeta \hat{\mathbf{z}} \times \mathbf{u}_h + w \partial_z \mathbf{u}_h + \nabla_h \frac{1}{2} |\mathbf{u}_h|^2 & \text{VectorInvariant,} \\ \zeta \hat{\mathbf{z}} \times \mathbf{u}_h - \mathbf{u}_h \partial_z w + \partial_z (w \mathbf{u}_h) + \nabla_h \frac{1}{2} |\mathbf{u}_h|^2 & \text{WENOVectorInvariant,} \end{cases} \quad (18)$$

433 where the “flux form” treats momentum advection in the same way as for the Nonhydrostat-
 434 icModel. The numerical implementation of the WENOVectorInvariant formulation, which
 435 leverages Weighted Essentially Non-Oscillatory (WENO) reconstructions to selectively and
 436 minimally dissipate enstrophy and the variance of divergence (see section 4), is described by
 437 [Silvestri, Wagner, Campin, et al. \(2024\)](#).

438 Tracer evolution is governed by the conservation law

$$\partial_t c = - \underbrace{(\mathbf{u} \cdot \nabla) c}_{\text{tracer advection}} - \underbrace{\nabla \cdot \mathbf{J}_c}_{\text{closure}} + \underbrace{S_c}_{\text{biogeochemistry}} + \underbrace{F_c}_{\text{forcing}}, \quad (19)$$

439 which is identical to NonhydrostaticModel except that background fields are not supported.
 440 Additionally, the velocity field \mathbf{u} can be prescribed rather than evolved.

441 Listing 8 implements a simulation of tidally-forced stratified flow over a series of
 442 randomly-positioned Gaussian seamounts. Results are plotted in figure 6.

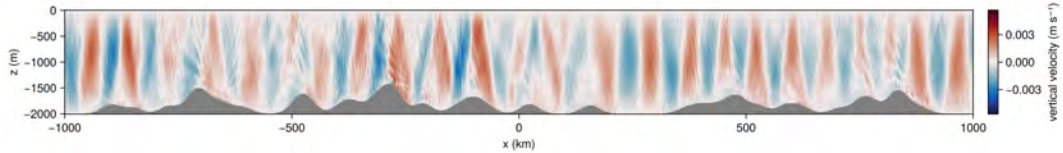


Figure 6: Vertical velocity of an internal wave field excited by tidally-forced stratified flow over superposition of randomly-positioned Gaussian seamounts, after 16 tidal periods.

```

1  using Oceananigans, Oceananigans.Units
2
3  grid = RectilinearGrid(size = (2000, 200),
4                        x = (-1000kilometers, 1000kilometers),
5                        z = (-2kilometers, 0),
6                        halo = (4, 4),
7                        topology = (Periodic, Flat, Bounded))
8
9  h0 = 100           # typical mountain height (m)
10 δ = 20kilometers # mountain width (m)
11 seamounts = 42
12 W = grid.Lx - 4δ
13 x0 = W .* (rand(seamounts) .- 1/2) # mountains' positions ∈ [-Lx/2+2δ, Lx/2-2δ]
14 h = h0 .* (1 .+ rand(seamounts)) # mountains' heights ∈ [h0, 2h0]
15
16 bottom(x) = -grid.Lz + sum(h[s] * exp(-(x - x0[s])^2 / 2δ^2) for s = 1:seamounts)
17 grid = ImmersedBoundaryGrid(grid, GridFittedBottom(bottom))
18
19 T2 = 12.421hours # period of M2 tide constituent
20 @inline tidal_forcing(x, z, t, p) = p.U2 * 2π / p.T2 * sin(2π / p.T2 * t)
21 u_forcing = Forcing(tidal_forcing, parameters=(; U2=0.1, T2=T2))
22
23 model = HydrostaticFreeSurfaceModel(; grid, tracers=:b, buoyancy=BuoyancyTracer(),
24                                     momentum_advection = WENO(),
25                                     tracer_advection = WENO(),
26                                     forcing = (; u = u_forcing))
27
28 bi(x, z) = 1e-5 * z
29 set!(model, b=bi)

```

Listing 8: Two-dimensional simulation of tidally-forced stratified flow over a superposition of randomly-positioned Gaussian seamounts. Results are shown in Figure 6.

3.2.1 Vertical mixing parameterizations

Oceananigans’ vertical mixing parameterizations are closures that predict the vertical fluxes of tracers and momentum. Depending on the parameterization, the evolution of auxiliary tracers like turbulent kinetic energy and the turbulent kinetic energy dissipation rate may also be simulated. Vertical mixing parameterizations are useful for hydrostatic simulations where vertical mixing is otherwise unresolved due to a coarse horizontal grid spacing. For example, such regional and global configurations, horizontal grid spacing typically varies from $O(100\text{ m})$ to $O(100\text{ km})$.

Listing 9 implements a simulation of wind-driven vertical mixing in a single column model using two parameterizations: CATKE (Wagner, Hillier, et al., 2025), which has one additional equation for the evolution of turbulent kinetic energy (TKE), and k - ϵ (Umlauf & Burchard, 2005), which has two additional equations for TKE and the TKE dissipation rate. Figure 7 plots the result, showing how k - ϵ undermixes compared to CATKE. This discrepancy in mixing rates is likely due to differences in how the models are calibrated. While all of CATKE’s parameters are jointly calibrated to 35 large eddy simulations (LES) that include surface wave effects (Wagner, Hillier, et al., 2025), k - ϵ parameters are calibrated one-by-one by referencing laboratory experiments and observations of increasing complexity (Umlauf & Burchard, 2003). Calibrating k - ϵ parameters similarly to CATKE is an interesting direction for future work.

3.3 Global ocean simulations with ClimaOcean

The HydrostaticFreeSurfaceModel can be used to simulate regional or global ocean circulation on rectilinear grids, latitude-longitude grids, and the tripolar grid (Murray, 1996) to cover the entirety of Earth’s global ocean. To illustrate global simulation with the HydrostaticFreeSurfaceModel, we implement a near-global simulation on a latitude-longitude

```

1 using Oceananigans
2 using Oceananigans.Units
3
4 function vertical_mixing_simulation(closure; N²=1e-5, Jb=1e-7, tx=-5e-4)
5     grid = RectilinearGrid(size=50, z=(-200, 0), topology=(Flat, Flat, Bounded))
6     buoyancy = BuoyancyTracer()
7
8     b_bcs = FieldBoundaryConditions(top=FluxBoundaryCondition(Jb))
9     u_bcs = FieldBoundaryConditions(top=FluxBoundaryCondition(tx))
10
11     if closure isa CATKEVerticalDiffusivity
12         tracers = (:b, :e)
13     elseif closure isa TKEDissipationVerticalDiffusivity
14         tracers = (:b, :e, :ε)
15     end
16
17     model = HydrostaticFreeSurfaceModel(; grid, closure, tracers, buoyancy,
18                                         boundary_conditions=(u=u_bcs, b=b_bcs))
19
20     bi(z) = N² * z
21     set!(model, b=bi)
22
23     simulation = Simulation(model, Δt=1minute, stop_time=24hours)
24     return run!(simulation)
25 end

```

Listing 9: Comparison of two vertical mixing parameterizations in the evolution of an initially linearly stratified boundary layer subjected to stationary surface fluxes of buoyancy and momentum. Results are shown in Figure 7.

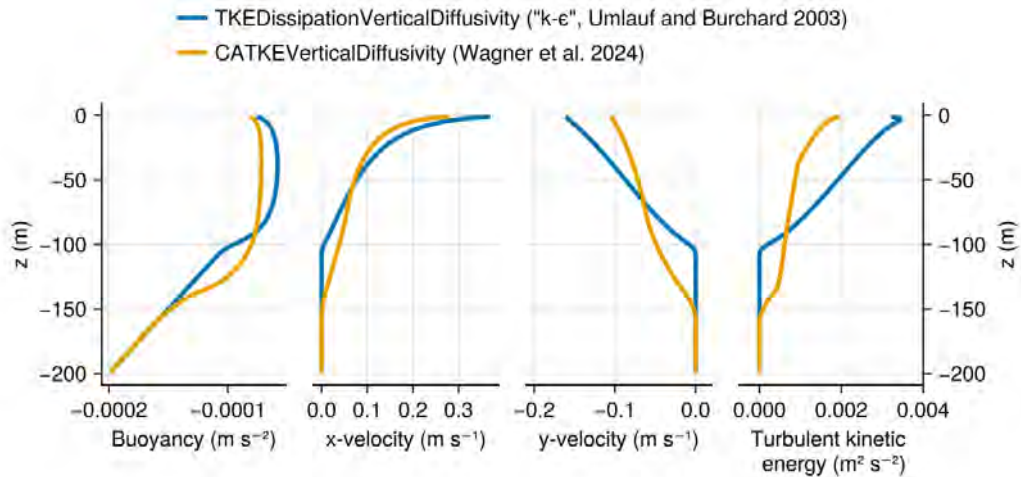


Figure 7: Results from two vertical mixing parameterizations: CATKE and $k-\epsilon$, implemented as described in Listing 9.

```

1 Nx, Ny, Nz = 4320, 1800, 40 # 1/12th degree
2 z_faces = ClimaOcean.exponential_z_faces(; Nz, depth=6000)
3 partition = Partition(8) # Distribute simulation across 8 GPUs
4 arch = Distributed(GPU(); partition)
5 grid = LatitudeLongitudeGrid(arch; size=(Nx, Ny, Nz), halo=(7, 7, 7),
6                               longitude=(0, 360), latitude=(-75, 75), z=z_faces)
7
8 bathymetry = ClimaOcean.regrid_bathymetry(grid) # based on ETOPO1
9 grid = ImmersedBoundaryGrid(grid, GridFittedBottom(bathymetry))
10
11 # Build an ocean simulation initialized to the ECCO state estimate on Jan 1, 1993
12 ocean = ClimaOcean.ocean_simulation(grid)
13 date = CFTIME.DateTimeProlepticGregorian(1993, 1, 1)
14 set!(ocean.model, T = ClimaOcean.ECCOMetadata(:temperature; date),
15       S = ClimaOcean.ECCOMetadata(:salinity; date))
16
17 # Near-global ocean simulation without no sea ice, forced by JRA55 reanalysis
18 backend = ClimaOcean.JRA55NetCDFBackend(41)
19 atmosphere = ClimaOcean.JRA55_prescribed_atmosphere(arch; backend)
20 coupled_model = ClimaOcean.OceanSeaIceModel(ocean; atmosphere)

```

Listing 10: A near-global simulation on a LatitudeLongitudeGrid distributed across 8 GPUs, leveraging ClimaOcean.

467 grid using ClimaOcean (Wagner, Silvestri, et al., 2025), which is a second package that
468 provides capabilities to compute interfacial fluxes between a prescribed atmosphere, a sea ice
469 model, and a hydrostatic ocean simulation implemented using Oceananigans. In ClimaOcean,
470 turbulent interfacial fluxes are computed using Monin-Obhukov similarity theory (Monin,
471 n.d.) following (Edson et al., 2014) for air-sea fluxes and (Grachev et al., 2007) for air-ice
472 fluxes. ClimaOcean additionally provides utilities for downloading and interfacing with
473 JRA55 reanalysis data (Tsujiro et al., 2018), building grids based on Earth bathymetry and
474 initializing simulations from the ECCO state estimate (Forget et al., 2015).

475 Part of a code that implements a near-global simulation with horizontal resolution of
476 1/12th degree, distributed over 8 GPUs, forced by JRA55 reanalysis and initialized from
477 the ECCO state estimate is shown in listing 10. The surface speed generated after 180 days
478 of simulation time is shown in figure 8. For more information about Oceananigans GPU
479 performance in global configurations, see Silvestri, Wagner, Constantinou, et al. (2024).

480 4 Finite volume spatial discretization

481 Oceananigans uses a finite volume method in which fields are represented discretely by
482 their average value over small local regions or “finite volumes” of the domain. Listing 11
483 discretizes $c = e^{xy}$ on three different grids that cover the unit square. At the finest resolution,
484 each cell-averaged value c_{ij}^{fine} is computed approximately using `set!` to evaluate e^{xy} at the
485 center of each finite volume, where i, j denote the x and y indices of the finite volumes.
486 At medium and coarse resolution, the c_{ij}^{medium} and c_{ij}^{coarse} are computed by averaging or
487 “regridding” fields discretized at a higher resolution. This computation produces three fields
488 with identical integrals over the unit square. For example, integrals are computed exactly by
489 summing discrete fields over all cells,

$$\int c dx dy = \sum_{i,j}^{1024,1024} \mathcal{V}_{ij}^{\text{fine}} c_{ij}^{\text{fine}} = \sum_{i,j}^{16,16} \mathcal{V}_{ij}^{\text{medium}} c_{ij}^{\text{medium}} = \sum_{i,j}^{4,4} \mathcal{V}_{ij}^{\text{coarse}} c_{ij}^{\text{coarse}}, \quad (20)$$

490 where \mathcal{V}_{ij} is the “volume” of the cell with indices i, j (more accurately an “area” in this
491 two-dimensional situation). Figure 9 visualizes the three fields.

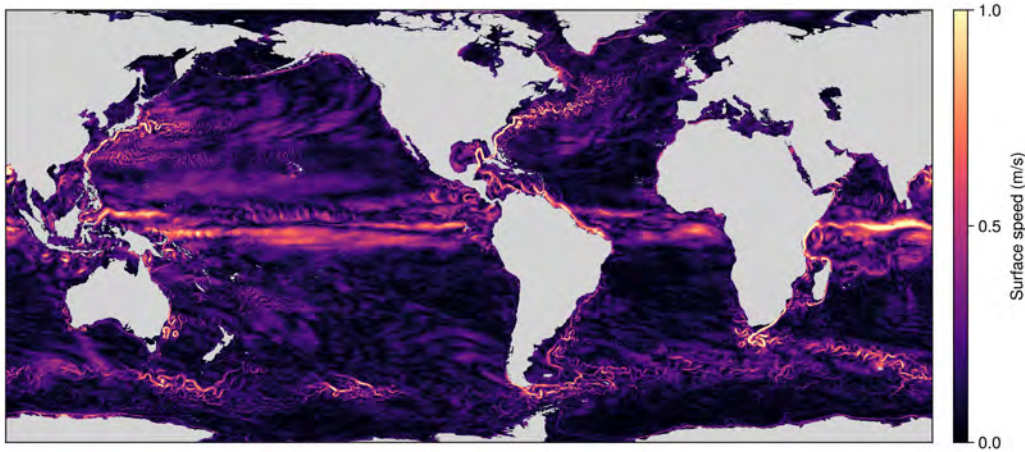


Figure 8: Surface speed in a near-global ocean simulation at 1/12th degree forced by JRA55 atmospheric reanalysis (Tsujino et al., 2018) initialized from the ECCO state estimate (Forget et al., 2015). Oceananigans can also cover the entirety of Earth’s global ocean using a tripolar grid (Murray, 1996).

```

1 topology = (Bounded, Bounded, Flat)
2 x = y = (0, 1)
3 c(x, y) = exp(x) * y
4
5 fine_grid = RectilinearGrid(size=(1024, 1024); x, y, topology)
6 c_fine = CenterField(fine_grid)
7 set!(c_fine, c)
8
9 medium_grid = RectilinearGrid(size=(16, 16); x, y, topology)
10 c_medium = CenterField(medium_grid)
11 regrid!(c_medium, c_fine)
12
13 coarse_grid = RectilinearGrid(size=(4, 4); x, y, topology)
14 c_coarse = CenterField(coarse_grid)
15 regrid!(c_coarse, c_medium)

```

Listing 11: Finite volume discretization of $e^x y$ on three grids over the unit square. The fields are visualized in figure 9. The meaning of the “Center” in “CenterField” is discussed below.

492 The discrete calculus and arithmetic operations required to solve the governing equations
493 of the NonhydrostaticModel and HydrostaticFreeSurfaceModel use the system of “staggered
494 grids” described by Arakawa (1977). Both models use “C-grid” staggering, where cells
495 for tracers, pressure, and the divergence of the velocity field $\nabla \cdot \mathbf{u}$ are co-located, and
496 cells for velocity components $\mathbf{u} = (u, v, w)$ are staggered by half a cell width in the x -,
497 y -, and z -direction, respectively. Listing 12 illustrates grid construction and notation for
498 a one-dimensional staggered grid with unevenly-spaced cells. Figure 10 visualizes 2- and
499 3-dimensional staggered grids, indicating the location of certain variables.

```

500
501 1 using Oceananigans
502 2
503 3
504 3 grid = RectilinearGrid(topology=(Bounded, Flat, Flat), size=4, x=[0, 0.2, 0.3, 0.7, 1])
505 4
506 5 u = Field{Face, Center, Center}(grid)
507 6 c = Field{Center, Center, Center}(grid)
508 7
509 8 xnodes(u) # [0.0, 0.2, 0.3, 0.7, 1.0]
510 9 xnodes(c) # [0.1, 0.25, 0.5, 0.85]
511 10 location(∂x(c)) # (Face, Center, Center)

```

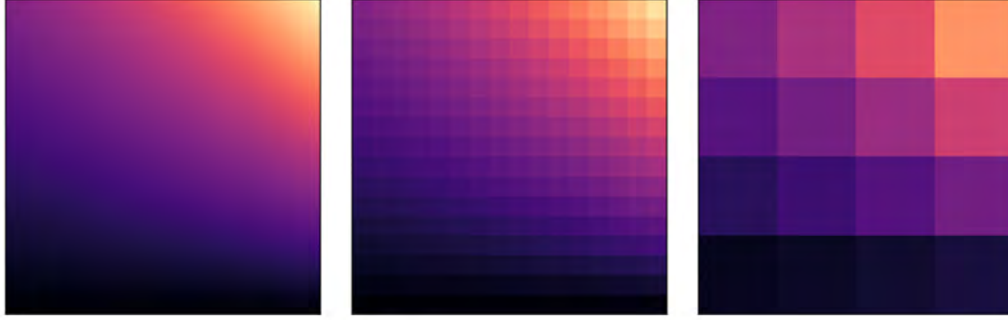


Figure 9: Finite volume discretization of $e^x y$ on the unit square at three different resolutions.

513

Listing 12: A one-dimensional staggered grid.

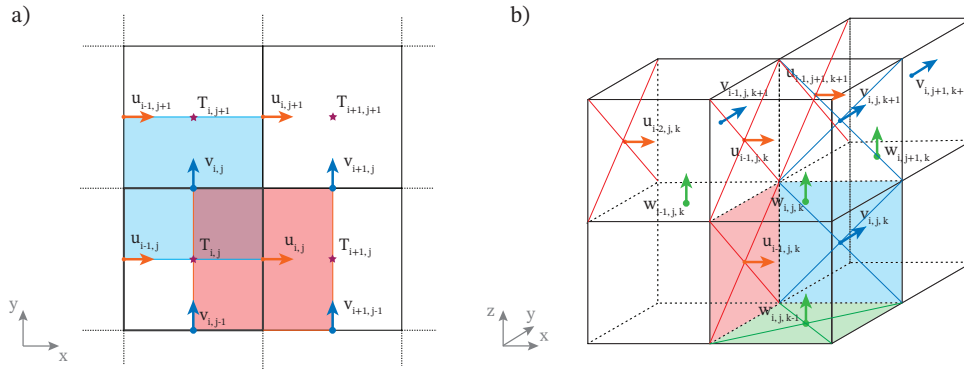


Figure 10: Locations of cell centers and interfaces on a two-dimensional (a) and three-dimensional (b) staggered grid. In (a), the red and blue shaded regions highlight the volumes in the dual u -grid and v -grid, located at (Face, Center, Center) and (Center, Face, Center), respectively. In (b), the shaded regions highlight the facial areas used in the fluxes computations, denoted with \mathcal{A}_x , \mathcal{A}_y , and \mathcal{A}_z .

514

4.1 A system of composable operators

515

516

517

518

519

520

521

522

523

$$1 \quad \delta_x^{fcc}(i, j, k, \text{grid}, c) = c[i, j, k] - c[i-1, j, k]$$

$$2 \quad \delta_x^{ccc}(i, j, k, \text{grid}, u) = u[i+1, j, k] - u[i, j, k]$$

525

526

where superscripts denote the location of the *result* of the operation. For example, the difference δ_x^{fcc} acts on fields located at ccc (meaning cell Center in the x , y and z directions

527 respectively). Complementary to the difference operators are reconstruction of “interpolation”
 528 operators,

529
 530
 531
 532
 533

```
1  $\mathbb{S}x^{fcc}(i, j, k, \text{grid}, c) = (c[i, j, k] + c[i-1, j, k]) / 2$ 
2  $\mathbb{S}x^{ccc}(i, j, k, \text{grid}, u) = (u[i+1, j, k] + u[i, j, k]) / 2$ 
```

535 The prefix arguments i, j, k, grid are more than convention: the prefix enables
 536 system for *composing* operators. For example, defining

537
 538
 539
 540
 541
 542
 543
 544

```
1  $\delta x^{fcc}(i, j, k, \text{grid}, f::\text{Function}, \text{args}...) =$   

2  $f(i, j, k, \text{grid}, \text{args}...) - f(i-1, j, k, \text{grid}, \text{args}...)$   

3  

4  $\delta x^{ccc}(i, j, k, \text{grid}, f::\text{Function}, \text{args}...) =$   

5  $f(i+1, j, k, \text{grid}, \text{args}...) - f(i, j, k, \text{grid}, \text{args}...)$ 
```

546 leads to a concise definition of the second-difference operator:

547
 548
 549
 550

```
1  $\delta^2 x^{ccc}(i, j, k, \text{grid}, f::\text{Function}, a...) = \delta x^{ccc}(i, j, k, \text{grid}, \delta x^{fcc}, f, a...)$ 
```

552 Operator composition is used throughout Oceananigans source code to implement stencil
 553 operations.

554 4.2 Tracer flux divergences, advection schemes, and reconstruction

555 The divergence of a tracer flux $\mathbf{J} = J_x \hat{\mathbf{x}} + J_y \hat{\mathbf{y}} + J_z \hat{\mathbf{z}}$ is discretized conservatively by
 556 the finite volume method via

$$\nabla \cdot \mathbf{J} \approx \frac{1}{\mathcal{V}_c} \left[\delta_x \underbrace{(\mathcal{A}_x J_x)}_{\text{fcc}} + \delta_y \underbrace{(\mathcal{A}_y J_y)}_{\text{cfc}} + \delta_z \underbrace{(\mathcal{A}_z J_z)}_{\text{ccf}} \right], \quad (21)$$

557 where $\delta_x, \delta_y, \delta_z$ are difference operators in x, y, z , \mathcal{V}_c denotes the volume of the tracer cells,
 558 $\mathcal{A}_x, \mathcal{A}_y$, and \mathcal{A}_z denote the areas of the tracer cell faces with surface normals $\hat{\mathbf{x}}, \hat{\mathbf{y}}$, and $\hat{\mathbf{z}}$,
 559 respectively. Equation (21) indicates the location of each flux component: fluxes into tracers
 560 cell at ccc are computed at the cell faces located at fcc, cfc, and ccf.

561 The advective tracer flux in (9) is written in “conservative form” using incompressibil-
 562 ity (2), and then discretized similarly to (21) to form

$$\mathbf{u} \cdot \nabla c = \nabla \cdot (\mathbf{u}c) \approx \frac{1}{\mathcal{V}_c} \left[\delta_x (\mathcal{A}_x u [c]_x) + \delta_y (\mathcal{A}_y v [c]_y) + \delta_z (\mathcal{A}_z w [c]_z) \right], \quad (22)$$

563 where $[c]_x$ denotes a *reconstruction* of c in the x -direction from its native location ccc to
 564 the tracer cell interface at fcc; $[c]_y$ and $[c]_z$ in (22) are defined similarly.

565 The advective fluxes $\mathbf{u}c$ must be computed on interfaces between tracer cells, where
 566 the approximate value of c must be reconstructed. (Velocity components like u must also
 567 be reconstructed on interfaces. Within the C-grid framework, we approximate u on tracer
 568 cell interfaces directly using the values u_{ijk} , which represent u averaged over a region
 569 encompassing the interface.) The simplest kind of reconstruction is Centered(order=2),
 570 which is equivalent to taking the average between adjacent cells,

$$\langle c \rangle_i = \frac{1}{2} (c_i + c_{i-1}), \quad (23)$$

571 where $\langle c \rangle_i$ denotes the centered reconstruction of c on the interface at $x = x_{i-1/2}$. Also
 572 in (23) the j, k indices are implied and we have suppressed the direction x to lighten the
 573 notation. Reconstructions stencils for Center(order= N) are automatically generated for

574 even N up to $N_{\max} = 12$, where N_{\max} is an adjustable parameter in the source code. All
 575 subsequent reconstructions are described in the x -direction only.

576 Centered schemes should be used when explicit dissipation justified by a *physical*
 577 rationale dominates at the grid scale. In scenarios where dissipation is needed solely for
 578 artificial reasons, we find applications for UpwindBiased schemes, which use an odd-order
 579 stencil biased against the direction of flow. For example, UpwindBiased(order=1) and
 580 UpwindBiased(order=3) schemes are written

$$u[c]_x^1 = \begin{cases} u c_{i-1} & \text{if } u > 0, \\ u c_i & \text{if } u < 0, \end{cases} \quad \text{and} \quad u[c]_x^3 = \begin{cases} u \frac{1}{6} (-c_{i-2} + 5c_{i-1} + 2c_i) & \text{if } u > 0, \\ u \frac{1}{6} (2c_{i-1} + 5c_i - c_{i+1}) & \text{if } u < 0, \end{cases} \quad (24)$$

581 where $[c]_x^N$ denotes N^{th} -order upwind reconstruction in the x -direction. (Note that $u[c]_x^N = 0$
 582 if $u = 0$.)

583 The compact form of equations (24) demonstrates how upwind schemes introduce vari-
 584 ance dissipation through numerical discretization. In particular, an UpwindBiased(order=1)
 585 reconstruction can be rewritten as a sum of a Centered(order=2) discrete advective flux and
 586 a discrete diffusive flux

$$u[c]_x^1 = u \frac{c_i + c_{i-1}}{2} - \kappa_1 \frac{c_i - c_{i-1}}{\Delta x}, \quad \text{where} \quad \kappa_1 = \frac{|u|\Delta x}{2}. \quad (25)$$

587 Reordering the UpwindBiased(order=3) advective flux in the same manner recovers a sum
 588 of a Centered(order=4) advective flux and a 4th-order hyperdiffusive flux, equivalent to a
 589 finite volume approximation of

$$uc + \kappa_3 \frac{\partial^3 c}{\partial x^3}, \quad \text{where} \quad \kappa_3 = \frac{|u|\Delta x^3}{12}. \quad (26)$$

590 UpwindBiased reconstruction can be always reordered to expose a sum of Centered recon-
 591 struction and a high-order diffusive flux with a velocity-dependent diffusivity. The diffusive
 592 operator associated with UpwindBiased(order=1) and UpwindBiased(order=3) is enough to
 593 offset the dispersive errors of the Centered component and, therefore, eliminate the artificial
 594 explicit diffusion needed for stability purposes. However, this approach does not scale to
 595 high order since the diffusive operator associated with a high order UpwindBiased scheme
 596 (5th, 7th, and so on), becomes quickly insufficient to eliminate spurious errors associated
 597 with the Centered component (Godunov, 1959).

598 The inability to achieve high order and, therefore, low dissipation motivated the im-
 599 plementation of Weighted, Essentially Non-Oscillatory (WENO) reconstruction (C. Shu,
 600 1997; C.-W. Shu, 2009). WENO is a non-linear reconstruction scheme that combines a
 601 set of odd-order linear reconstructions obtained by stencils that are shifted by a value s
 602 relative to the canonical UpwindBiased stencil, using a weighting scheme for each stencil
 603 that depends on the smoothness of the reconstructed field c . Since the constituent stencils
 604 are lower-order than the WENO order, this strategy yields a scheme whose order of accuracy
 605 adapts depending on the smoothness of the reconstructed field. In smooth regions high-order
 606 is retained, while the order quickly decreases in the presence of noisy regions, decreasing the
 607 order of the associated diffusive operator. WENO proves especially useful for high-resolution,
 608 turbulence-resolving simulations (either at meter or planetary scales) without requiring any
 609 additional explicit artificial dissipation (Pressel et al., 2017; Silvestri, Wagner, Campin, et
 610 al., 2024).

611 To illustrate how WENO works we consider a fifth-order WENO scheme for $u > 0$,

$$\{c\}^5 = \gamma_0 [c]^{3,0} + \gamma_1 [c]^{3,1} + \gamma_2 [c]^{3,2}, \quad (27)$$

612 where the notation $[c]^{3,s}$ denotes an UpwindBiased stencil *shifted* by s indices, such that
 613 $[c]^3 \stackrel{\text{def}}{=} [c]^{3,0}$. The shifted upwind stencils $[c]_i^{N,s}$ evaluated at index i are defined

$$[c]_i^{3,s} = \frac{1}{6} \begin{cases} -c_{i-1} + 5c_i + 2c_{i+1} & \text{for } s = -1, \\ 2c_{i-2} + 5c_{i-1} - c_i & \text{for } s = 0, \\ 2c_{i-3} - 7c_{i-2} + 11c_{i-1} & \text{for } s = 2. \end{cases} \quad (28)$$

614 The weights $\gamma_s(c)$ are determined by a smoothness metric that produces $\{c\}^5 \approx [c]^5$ when c is
 615 smooth, but limits to the more diffusive $\{c\}^5 \approx [c]^3$ when c changes abruptly. Thus WENO
 616 adaptively introduces dissipation as needed based on the smoothness of c , yielding stable
 617 simulations with a high effective resolution that require no artificial dissipation. WENO can
 618 alternatively be interpreted as adding an implicit hyperviscosity that adapts from low- to
 619 high-order depending on the local nature of the solution. To compute the weights $\gamma_s(c)$, we
 620 use the WENO-Z formulation (Balsara & Shu, 2000).

621 The properties of Centered, UpwindBiased, and WENO reconstruction are investigated
 622 by listing 13, which simulates the advection of a top hat tracer distribution. The results are
 623 plotted in figure 11.

```
624 1 using Oceananigans
625 2
626 3 grid = RectilinearGrid(size=128; x=(-4, 8), halo=6, topology=(Periodic, Flat, Flat))
627 4 advection = WENO(order=9) # Centered(order=2), UpwindBiased(order=3)
628 5 velocities = PrescribedVelocityFields(u=1)
629 6 model = HydrostaticFreeSurfaceModel(; grid, velocities, advection, tracers=:c)
630 7
631 8 top_hat(x) = abs(x) > 1 ? 0 : 1
632 9 set!(model, c = top_hat)
633 10
634 11 simulation = Simulation(model, Δt=1/grid.Nx, stop_time=4)
635 12 run!(simulation)
636
637
638
```

Listing 13: A script that advects a top hat tracer profile in one-dimension with a constant prescribed velocity. We use halo=6 to accommodate schemes up to WENO(order=11).

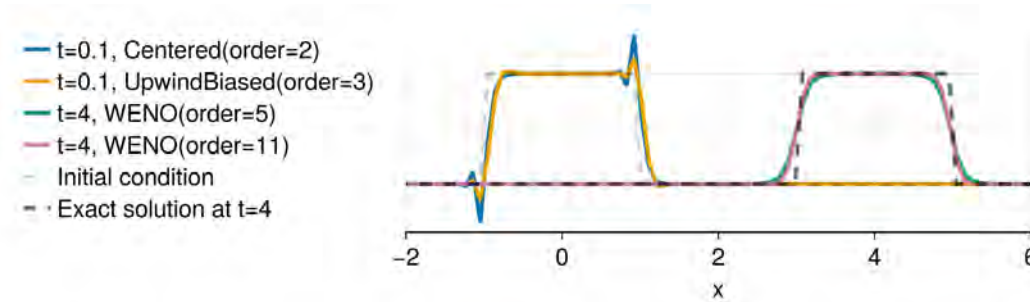


Figure 11: Advection of a top hat tracer distribution in one-dimension using various advection schemes. Centered and Upwind

640 4.2.1 Discretization of momentum advection

641 The discretization of momentum advection with a flux form similar to (22) is more
 642 complex than the tracer case because both the advecting velocity and advected velocity
 643 require reconstruction. We use the method described by Ghosh and Baeder (2012) and Pressel

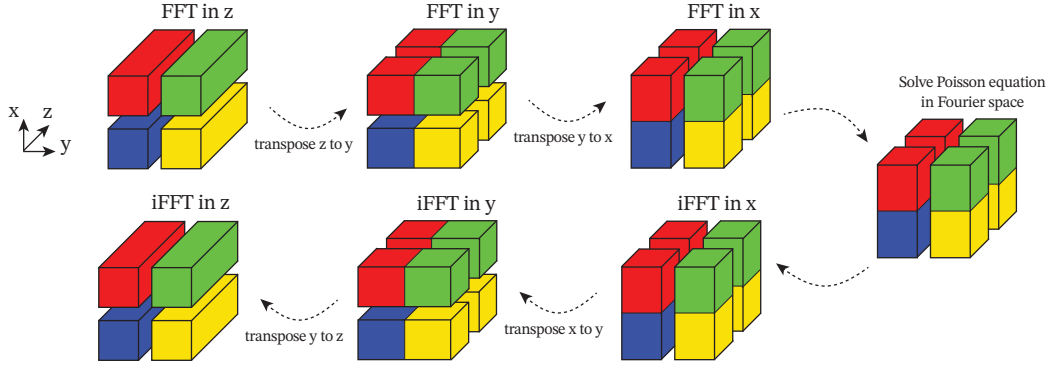


Figure 12: A schematic showing the distributed Poisson solver procedure with a pencil parallelization that divides the domain in two ranks in both x and y . The schematic highlights the data layout in the ranks during each operation.

644 [et al. \(2015\)](#), wherein advecting velocities are constructed with a high-order Centered scheme
 645 when the advected velocity component is reconstructed with a high-order UpwindBiased
 646 or WENO scheme. We have also developed a novel WENO-based method for discretizing
 647 momentum advection in the rotational or “vector invariant” form especially appropriate for
 648 representing mesoscale and submesoscale turbulent advection on curvilinear grids ([Silvestri,
 649 Wagner, Campin, et al., 2024](#)).

650 5 Parallelization

651 Oceananigans supports distributed computations with slab and pencil domain decompo-
 652 sition. The interior domain is extended using “halo” or “ghost” cells that hold the results of
 653 interprocessor boundaries. “halo” cells are updated before the computation of tendencies
 654 through asynchronous send / receive operations using the message passing interface (MPI)
 655 Julia library ([Byrne et al., 2021](#)). For a detailed description of the parallelization strategy of
 656 the `HydrostaticFreeSurfaceModel`; see [Silvestri, Wagner, Constantinou, et al. \(2024\)](#). The
 657 `NonhydrostaticModel` implements the same overlap of communication and computation for
 658 halo exchange before the calculation of tendencies. For the FFT-based three-dimensional
 659 pressure solver, we implement a transpose algorithm that switches between x -local, y -local,
 660 and z -local configurations to compute efficiently the discrete transforms. The transpose
 661 algorithm for the distributed FFT solver is shown in figure 12.

662 6 Conclusions

663 This paper describes GPU-based ocean modeling software called “Oceananigans” written
 664 in the high-level Julia programming language. Oceananigans enables high resolution simu-
 665 lations of oceanic motion at any scale with an innovative user interface design that makes
 666 simple simulations easy and complex, creative simulations possible. The current state of
 667 Oceananigans realizes a particular strategy for improving dynamical cores: simple, C-grid,
 668 WENO numerics for turbulence resolving simulations coupled to the raw power of GPU
 669 acceleration.

670 Using GPUs enables high-resolution simulations on few resources — such as a single GPU
 671 instance on the cloud — increasing access to ocean modeling. But it also enables a new class
 672 of very high resolution simulations. For example, on the Perlmutter supercomputer ([National
 673 Energy Research Scientific Computing Center, 2025](#)), it is currently possible to complete a
 674 100-member ensemble of century-long global ocean simulations at 10 kilometer resolution in

675 10 days of wall time — thereby resolving mesoscale turbulent mixing, a prominent bias in
 676 ocean models and a fundamental process missing from most climate simulations today. These
 677 new capabilities address uncertainty in ocean heat and carbon uptake in climate projections.

678 Oceananigans is designed for composition with external packages, which has fostered the
 679 development of a number of auxiliary packages. For example, OceanBioME (Strong-Wright
 680 et al., 2023) implements Oceananigans-compatible biogeochemistry models, oriented towards
 681 ecosystem dynamics and compatible with both the hydrostatic and nonhydrostatic models.
 682 A second biogeochemistry package is also under development for climate simulations. The
 683 Oceanostics (Chor et al., 2025) package implements complex diagnostics in Oceananigans
 684 syntax, useful for online and offline analysis of large eddy simulations.

685 A next step is to couple ocean models built with Oceananigans to prognostic atmosphere
 686 models, including the Climate Modeling Alliance atmosphere dynamical core (Yatunin et al.,
 687 2025) and the simpler SpeedyWeather (Kl ower et al., 2024). A further possibility, enabled
 688 by Oceananigans GPU capabilities, is to couple to hybrid physics/AI atmosphere models
 689 (Kochkov et al., 2024), or fully-AI atmosphere models like ACE (Watt-Meyer et al., 2023,
 690 2024) and GraphCast (Lam et al., 2023). A sea ice model called ClimaSeaIce, which uses
 691 the same finite volume engine underpinning Oceananigans, is under active development to
 692 support coupled ocean-sea-ice simulations. There is also an ongoing effort to use Enzyme
 693 (Moses et al., 2021) to develop an adjoint for Oceananigans, and to more generally use
 694 autodifferentiation to compute the gradients of cost functions that invoke Oceananigans
 695 simulations.

696 Each achievement — groundbreaking performance, physics flexibility, or an innovative
 697 design — would, on their own, enable scientific breakthroughs. This matters because ocean
 698 modeling software will have to continue to evolve rapidly to keep pace with the advancing
 699 state of computational science to remain cutting-edge: to continue to use the world’s largest
 700 supercomputers, to present the most productive possible abstractions for both users and
 701 developers, and to enable the next generation of parameterizations and AI-based model
 702 components.

703 Appendix A Time stepping and time discretization

704 In this section we describe time stepping methods and time discretization options for
 705 the NonhydrostaticModel and the HydrostaticFreeSurfaceModel.

706 A1 Time discretization for tracers

707 Tracers are stepped forward with similar schemes in the NonhydrostaticModel and the
 708 HydrostaticFreeSurfaceModel, each of which includes optional implicit treatment of vertical
 709 diffusion terms. Equation (9) is abstracted into two components,

$$\partial_t c = G_c + \partial_z (\kappa_z \partial_z c), \quad (\text{A1})$$

710 where, if specified, κ_z is the vertical diffusivity of c to be treated with a VerticallyIm-
 711 plicitTimeDiscretization, and G_c is the remaining component of the tracer tendency from
 712 equation 9. (Vertical diffusion treated with an ExplicitTimeDiscretization is also absorbed
 713 into G_c .) We apply a semi-implicit time discretization of vertical diffusion to approximate
 714 integral of (A1) from t^m to t^{m+1} ,

$$(1 - \Delta t \partial_z \kappa_z^m \partial_z) c^{m+1} = c^m + \int_{t^m}^{t^{m+1}} G_c dt, \quad (\text{A2})$$

715 where $\Delta t \stackrel{\text{def}}{=} t^{m+1} - t^m$. The tendency integral $\int_{t^m}^{t^{m+1}} G_c dt$ is evaluated either using a
 716 “quasi”-second order Adams-Bashforth scheme (QAB2, which is actually first-order *lets add a*
 717 *reference*), or a low-storage third-order Runge-Kutta scheme (RK3). For QAB2, the integral

718 in (A2) spans the entire time-step and takes the form

$$\frac{1}{\Delta t} \int_{t^m}^{t^{m+1}} G_c dt \approx \left(\frac{3}{2} + \chi\right) G_c^m - \left(\frac{1}{2} + \chi\right) G_c^{m-1}, \quad (\text{A3})$$

719 where χ is a small parameter, chosen by default to be $\chi = 0.1$. QAB2 requires one tendency
 720 evaluation per time-step. For RK3, the indices $m = (1, 2, 3)$ correspond to *substages*, and
 721 the integral in (A2) takes the form

$$\frac{1}{\Delta t} \int_{t^m}^{t^{m+1}} G_c dt \approx \gamma^m G_c^m - \zeta^m G_c^{m-1}, \quad (\text{A4})$$

722 where $\gamma = (8/15, 5/12, 3/4)$ and $\zeta = (0, 17/60, 5/12)$ for $m = (1, 2, 3)$ respectively. RK3
 723 requires three evaluations of the tendency G_c per time-step. RK3 is self-starting because
 724 $\zeta^1 = 0$, while QAB2 must be started with a forward-backwards Euler step (the choice
 725 $\chi = -1/2$ in (A3)). Equation (A2) is solved with a tridiagonal algorithm following a second-
 726 order spatial discretization of $\partial_z \kappa_z^n \partial_z c^{m+1}$ — either once per time-step for QAB2, or three
 727 times for each of the RK3’s three stages.

728 VerticallyImplicitTimeDiscretization permits longer time-steps when using fine vertical
 729 spacing. Listing 14 illustrates the differences between vertically-implicit and explicit time
 730 discretization using one-dimensional diffusion of by a top-hat diffusivity profile. The results
 731 are shown in figure A1.

732
 733
 734
 735
 736
 737
 738
 739
 740
 741
 742

```

1 using Oceananigans
2
3 grid = RectilinearGrid(size=20, z=(-2, 2), topology=(Flat, Flat, Bounded))
4 time_discretization = VerticallyImplicitTimeDiscretization()
5  $\kappa(z, t) = \exp(-z^2)$ 
6 closure = VerticalScalarDiffusivity(time_discretization;  $\kappa$ )
7 model = HydrostaticFreeSurfaceModel(; grid, closure, tracers=:c)

```

Listing 14: Diffusion of a tracer by a top hat tracer diffusivity profile using various time steps and time discretizations.

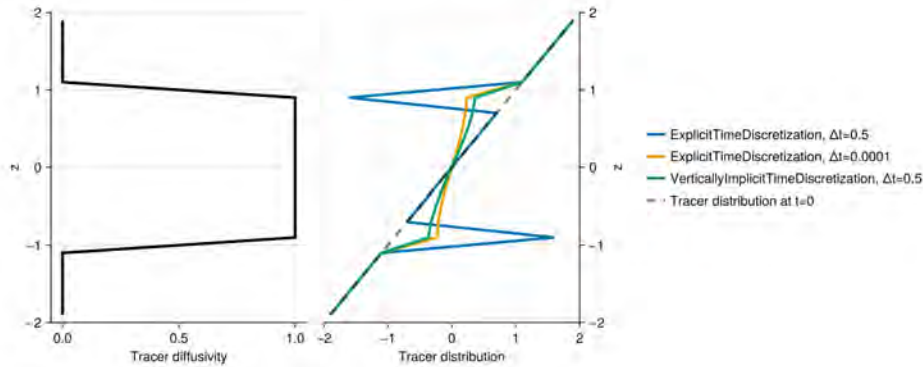


Figure A1: Simulations of tracer diffusion by a top hat diffusivity profile using various choices of time-discretization and time-step size. With a long time-step of $\Delta t = 0.5$, ExplicitTimeDiscretization is unstable while VerticallyImplicitTimeDiscretization is stable. Let the vertically-implicit solution depends on the long time-step $\Delta t = 0.5$, as revealed by comparison with ExplicitTimeDiscretization using $\Delta t = 10^{-4}$.

A2 The pressure correction method for momentum in NonhydrostaticModel

The NonhydrostaticModel uses a pressure correction method for the momentum equation (6) that ensures $\nabla \cdot \mathbf{u} = 0$. We rewrite (6) as

$$\partial_t \mathbf{u} = -\nabla p + b \hat{\mathbf{z}} + \mathbf{G}_u + \partial_z (\nu_z \partial_z \mathbf{u}), \quad (\text{A5})$$

where, if specified, ν_z is the vertical component of the viscosity that will be treated with a vertically-implicit time discretization, ∇p is the total pressure gradient, and \mathbf{G}_u is the rest of the momentum tendency. We decompose p into a “hydrostatic anomaly” p' tied to the density anomaly ρ' , and a nonhydrostatic component \tilde{p} , such that

$$p = \tilde{p} + p', \quad \text{where} \quad \partial_z p' \stackrel{\text{def}}{=} b. \quad (\text{A6})$$

By computing p_h in (A6), we recast (A5) without b and with $\nabla p = \nabla p_n + \nabla_h p_h$. Next, integrating (A5) in time from t^m to t^{m+1} yields

$$\mathbf{u}^{m+1} = \mathbf{u}^m + \int_{t^m}^{t^{m+1}} [\mathbf{G}_u - \nabla \tilde{p} + \partial_z (\nu_z \partial_z \mathbf{u})] dt. \quad (\text{A7})$$

Next we introduce the predictor velocity $\tilde{\mathbf{u}}$, defined such that

$$(1 - \Delta t \partial_z \nu_z^m \partial_z) \tilde{\mathbf{u}} = \mathbf{u}^m + \int_{t^m}^{t^{m+1}} \mathbf{G}_u dt, \quad (\text{A8})$$

or in other words, defined as a velocity-like field that cannot feel nonhydrostatic pressure gradient $\nabla \tilde{p}$. Equation (A8) uses a semi-implicit treatment of vertical momentum diffusion which is similar but slightly different to the treatment of tracer diffusion in (A2),

$$\int_{t^m}^{t^{m+1}} \partial_z (\nu_z \partial_z \mathbf{u}) dt \approx \Delta t \partial_z (\nu_z^m \partial_z \tilde{\mathbf{u}}). \quad (\text{A9})$$

The integral in (A8) is evaluated with the same methods used for tracers — either (A3) for QAB2 or (A4) when using RK3. With a second-order discretization of vertical momentum diffusion, the predictor velocity in (A8) may be computed with a tridiagonal solver.

Introducing a fully-implicit time discretization for \tilde{p} ,

$$\int_{t^m}^{t^{m+1}} \nabla \tilde{p} dt \approx \Delta t \nabla \tilde{p}^{m+1}, \quad (\text{A10})$$

and inserting (A10) into (A8), we derive the pressure correction to the predictor velocity,

$$\mathbf{u}^{m+1} - \tilde{\mathbf{u}} = -\Delta t \nabla \tilde{p}^{m+1}. \quad (\text{A11})$$

The final ingredient needed to complete the pressure correction scheme is an equation for the nonhydrostatic pressure \tilde{p}_n^{m+1} . For this we form $\nabla \cdot (\text{A11})$ and use $\nabla \cdot \mathbf{u}^{m+1} = 0$ to obtain a Poisson equation for \tilde{p}_n^{m+1} ,

$$\nabla^2 \tilde{p}_n^{m+1} = \frac{\nabla \cdot \tilde{\mathbf{u}}}{\Delta t}. \quad (\text{A12})$$

Boundary conditions for equation (A12) may be derived by evaluating $\hat{\mathbf{n}} \cdot (\text{A7})$ on the boundary of the domain.

On RectilinearGrids, we solve (A12) using an eigenfunction expansion of the discrete second-order Poisson operator ∇^2 evaluated via the fast Fourier transform (FFT) in equispaced directions (Schumann & Sweet, 1988) plus a tridiagonal solve in variably-spaced directions. With the FFT-based solver, boundary conditions on \tilde{p}_n^{m+1} are accounted for by enforcing $\hat{\mathbf{n}} \cdot \tilde{\mathbf{u}} = \hat{\mathbf{n}} \cdot \mathbf{u}^{m+1}$ on boundary cells — which is additional and separate from

771 the definition $\tilde{\mathbf{u}}$ in (A9). This alteration of $\tilde{\mathbf{u}}$ on the boundary implicitly contributes the
 772 appropriate terms that account for inhomogeneous boundary-normal pressure gradients
 773 $\hat{\mathbf{n}} \cdot \nabla \tilde{p}^{m+1} \neq 0$ to the right-hand-side of (A12) during the computation of $\nabla \cdot \tilde{\mathbf{u}}$.

774 A preconditioned conjugate gradient iteration may be used on non-rectilinear grids,
 775 including complex domains. For domains that immerse an irregular boundary within a
 776 RectilinearGrid, we have implemented an efficient, rapidly-converging preconditioner that
 777 leverages the FFT-based solver with masking applied to immersed cells. The FFT-based
 778 preconditioner for solving the Poisson equation in irregular domains will be described in a
 779 forthcoming paper.

780 **A3 Time discretization of the HydrostaticFreeSurfaceModel**

781 The HydrostaticFreeSurfaceModel uses a linear free surface formulation paired with
 782 a geopotential vertical coordinate that may be integrated in time using either a fully
 783 ExplicitFreeSurface, an ImplicitFreeSurface utilizing a two-dimensional elliptical solve, or a
 784 SplitExplicitFreeSurface. The latter free surface solver can also be used to solve the primitive
 785 equations with a non-linear free surface formulation and a free-surface following vertical
 786 coordinate (the z^* vertical coordinate, Adcroft & Campin, 2004). For brevity, we describe
 787 here only the SplitExplicitFreeSurface, which is the most generally useful method. The
 788 SplitExplicitFreeSurface substeps the depth-integrated or “barotropic” horizontal velocity
 789 \mathbf{U}_h along with the free surface displacement η using a short time step while and the depth-
 790 dependent, “baroclinic” velocities, along with tracers, are relatively stationary.

791 The barotropic horizontal transport \mathbf{U}_h is defined

$$\mathbf{U}_h \stackrel{\text{def}}{=} \int_{-H}^{\eta} \mathbf{u}_h \, dz, \quad (\text{A13})$$

792 where $\mathbf{u}_h = (u, v)$ is the total horizontal velocity and H is the depth of the fluid.

793 Similarly integrating the horizontal momentum equations (17) from $z = -H$ to $z = \eta$
 794 yields an evolution equation for \mathbf{U}_h ,

$$\partial_t \mathbf{U}_h = -g(H + \eta) \nabla_h \eta + \int_{-H}^{\eta} \mathbf{G}_{uh} \, dz, \quad (\text{A14})$$

795 where \mathbf{G}_{uh} includes all the tendency terms that evolve “slowly” compared to the barotropic
 796 mode:

$$\mathbf{G}_{uh} = -(\mathbf{u} \cdot \nabla) \mathbf{u}_h - \mathbf{f} \times \mathbf{u} - \nabla \cdot \boldsymbol{\tau} + \mathbf{F}_h. \quad (\text{A15})$$

797 The evolution equation for the free surface is obtained by integrating the continuity equa-
 798 tion (15) in z to obtain $\nabla \cdot \mathbf{U}_h = -w|_{z=\eta}$, and inserting this into (16) to find

$$\partial_t \eta = -\nabla_h \cdot \mathbf{U}_h. \quad (\text{A16})$$

799 The pair of equations (A14) and (A16) characterize the evolution of the barotropic mode,
 800 which involves faster time-scales than the baroclinic mode evolution described by equations
 801 (17). To resolve both modes, we use a split-explicit algorithm where the barotropic mode is
 802 advanced in time using a smaller time-step than the one used for three-dimensional baroclinic
 803 variables. In particular, a predictor three-dimensional velocity is evolved without accounting
 804 for the barotropic mode evolution, using the QAB2 scheme described by A3. We denote this
 805 “predictor” velocity, again, with a tilde as done in section A2.

$$(1 - \Delta t \partial_z \nu_z^m \partial_z) \tilde{\mathbf{u}}_h - \mathbf{u}_h^m \approx \int_{t^m}^{t^{m+1}} \mathbf{G}_{uh} \, dt. \quad (\text{A17})$$

806 We then compute the barotropic mode evolution by sub-stepping M times the barotropic
 807 equations using a forward-backward time-stepping scheme and a time-step $\Delta \tau = \Delta t / N$,

$$\eta^{n+1} - \eta^n = -\Delta \tau \nabla_h \cdot \mathbf{U}_h^n, \quad (\text{A18})$$

808

$$\mathbf{U}_h^{n+1} - \mathbf{U}_h^n = -\Delta\tau \left[g(H + \eta) \nabla_h \eta^{n+1} - \frac{1}{\Delta t} \int_{-H}^{\eta} \int_{t^m}^{t^{m+1}} \mathbf{G}_{uh} dt dz \right]. \quad (\text{A19})$$

809

810

The slow tendency terms are frozen in time during substepping. The barotropic quantities are averaged within the sub-stepping with

$$\bar{\mathbf{U}}_h = \sum_{n=1}^M a_n \mathbf{U}_h^n, \quad \bar{\eta} = \sum_{n=1}^M a_n \eta^n, \quad (\text{A20})$$

811

812

813

814

815

816

where M is the number of substeps per baroclinic step, and a_n are the weights are calculated from the provided averaging kernel. The default choice of averaging kernel is the minimal dispersion filters developed by Shchepetkin and McWilliams (2005). The number of substeps M is calculated to center the averaging kernel at t^{m+1} . As a result, the barotropic subcycling overshoots the baroclinic step, i.e. $M > N$ with a maximum of $M = 2N$. Finally, the barotropic mode is reconciled to the baroclinic mode with a correction step

$$\mathbf{u}_h^{m+1} = \tilde{\mathbf{u}}_h + \frac{1}{H + \eta} \left(\bar{\mathbf{U}}_h - \int_{-H}^{\eta} \tilde{\mathbf{u}}_h dz \right). \quad (\text{A21})$$

817

818

The barotropic variables are then reinitialized for evolution in the next barotropic mode evolution using the time-averaged $\bar{\eta}$ and $\bar{\mathbf{U}}_h$.

819

Appendix B Table of numerical examples

Description	Code	Visualization
2D turbulence using WENO(order=9) advection	listing 1	fig. 1
2D turbulence with moving tracer source	listing 2	fig. 1
DNS and LES of flow around a cylinder at various Re	listing 4	fig. 2
DNS of cabbeling in freshwater	listing 5	fig. 3
LES of the Eady problem with WENO(order=9)	listing 6	fig. 4
Tidally-oscillating flow past Three Tree Point	listing 7	fig. 5
Internal waves generated by tidal forcing over bathymetry	listing 8	fig. 6
Comparison of vertical mixing parameterizations	listing 9	fig. 7
Near-global ocean simulation with ClimaOcean	listing 10	fig. 8
Visualization of the finite volume discretization	listing 11	fig. 9
One-dimensional advection of a top-hat tracer profile	listing 13	fig. 11
Tracer diffusion with various time discretizations	listing 14	fig. A1

821

Open Research Section

822

823

824

825

826

Oceananigans is available at the GitHub repository github.com/CliMA/Oceananigans.jl. Oceananigans documentation lives at <https://clima.github.io/OceananigansDocumentation>. All the scripts that reproduce the simulations and figures in this paper are available at the GitHub repository github.com/glwagner/OceananigansPaper. Visualizations were made using Makie.jl (Danisch & Krumbiegel, 2021).

827

Acknowledgments

828

This project is supported by Schmidt Sciences, LLC and by the National Science Foundation

829 grant AGS-1835576. N.C.C. is additionally supported by the Australian Research Council
 830 under the Center of Excellence for the Weather of the 21st Century CE230100012 and the
 831 Discovery Project DP240101274.

832 References

- 833 Adcroft, A., & Campin, J.-M. (2004). Rescaled height coordinates for accurate representation
 834 of free-surface flows in ocean circulation models. *Ocean Modelling*, *7*(3-4), 269–284.
- 835 Arakawa, A. (1977). Computational design of the basic dynamical processes of the UCLA
 836 general circulation model. *Methods in Computational Physics/Academic Press*.
- 837 Balsara, D., & Shu, C. (2000). Monotonicity preserving weighted essentially non-oscillatory
 838 schemes with increasingly high order of accuracy. *Journal of Computational Physics*,
 839 *160*(2), 405–452. doi: 10.1006/jcph.2000.6443
- 840 Besard, T., Foket, C., & De Sutter, B. (2018). Effective extensible programming: unleashing
 841 Julia on GPUs. *IEEE Transactions on Parallel and Distributed Systems*, *30*(4), 827–
 842 841.
- 843 Bezanson, J., Edelman, A., Karpinski, S., & Shah, V. B. (2017). Julia: A fresh approach to
 844 numerical computing. *SIAM review*, *59*(1), 65–98.
- 845 Boccaletti, G., Ferrari, R., & Fox-Kemper, B. (2007). Mixed layer instabilities and restratifi-
 846 cation. *Journal of Physical Oceanography*, *37*(9), 2228–2250.
- 847 Bou-Zeid, E., Meneveau, C., & Parlange, M. (2005). A scale-dependent Lagrangian dynamic
 848 model for large eddy simulation of complex turbulent flows. *Physics of fluids*, *17*(2).
- 849 Bryan, K. (1969). A numerical method for the study of the circulation of the world ocean.
 850 *Journal of Computational Physics*, *135*(2), 154–169.
- 851 Burns, K. J., Vasil, G. M., Oishi, J. S., Lecoanet, D., & Brown, B. P. (2020). Dedalus: A
 852 flexible framework for numerical simulations with spectral methods. *Physical Review
 853 Research*, *2*(2), 023068.
- 854 Byrne, S., Wilcox, L. C., & Churavy, V. (2021). MPI.jl: Julia bindings for the Message
 855 Passing Interface. In *Proceedings of the JuliaCon Conferences* (Vol. 1, p. 68). doi:
 856 10.21105/jcon.00068
- 857 Callies, J., & Ferrari, R. (2018). Baroclinic instability in the presence of convection. *Journal
 858 of Physical Oceanography*, *48*(1), 45–60.
- 859 Chassignet, E. P., & Xu, X. (2017). Impact of horizontal resolution (1/12 to 1/50) on Gulf
 860 Stream separation, penetration, and variability. *Journal of Physical Oceanography*,
 861 *47*(8), 1999–2021.
- 862 Chassignet, E. P., & Xu, X. (2021). On the importance of high-resolution in large-scale
 863 ocean models. *Advances in Atmospheric Sciences*, *38*, 1621–1634.
- 864 Chor, T., Constantinou, N. C., Bisits, J. I., Wagner, G. L., Ramadhan, A., Zheng, Z., &
 865 Whitley, V. (2025). *Oceanostics.jl*. Zenodo. Retrieved from [https://doi.org/
 866 10.5281/zenodo.8280754](https://doi.org/10.5281/zenodo.8280754) doi: 10.5281/zenodo.8280754
- 867 Churavy, V. (2024). *KernelAbstractions.jl*. Zenodo. Retrieved from [https://doi.org/
 868 10.5281/zenodo.13773520](https://doi.org/10.5281/zenodo.13773520) doi: 10.5281/zenodo.13773520
- 869 Cox, M. D. (1984). *A primitive equation, 3-dimensional model of the ocean* (Tech. Rep.
 870 No. 1). Princeton, NJ: NOAA Geophysical Fluid Dynamics Laboratory.
- 871 Craik, A. D., & Leibovich, S. (1976). A rational model for Langmuir circulations. *Journal
 872 of Fluid Mechanics*, *73*(3), 401–426.
- 873 Danilov, S., Sidorenko, D., Wang, Q., & Jung, T. (2017). The finite-volume sea ice–ocean
 874 model (FESOM2). *Geoscientific Model Development*, *10*(2), 765–789.
- 875 Danisch, S., & Krumbiegel, J. (2021). Makie.jl: Flexible high-performance data visualization
 876 for Julia. *Journal of Open Source Software*, *6*(65), 3349. doi: 10.21105/joss.03349
- 877 Dong, J., Fox-Kemper, B., Wenegrat, J. O., Bodner, A. S., Yu, X., Belcher, S., & Dong,
 878 C. (2024). Submesoscales are a significant turbulence source in global ocean surface
 879 boundary layer. *Nature Communications*, *15*(1), 9566.
- 880 Eady, E. T. (1949). Long waves and cyclone waves. *Tellus*, *1*(3), 33–52.

- 881 Edson, J. B., Jampana, V., Weller, R. A., Bigorre, S. P., Plueddemann, A. J., Fairall, C. W.,
 882 ... Hersbach, H. (2014). On the exchange of momentum over the open ocean. *Journal*
 883 *of Physical Oceanography*, *44*(9), 1589.
- 884 Forget, G., Campin, J.-M., Heimbach, P., Hill, C., Ponte, R., & Wunsch, C. (2015). ECCO
 885 version 4: An integrated framework for non-linear inverse modeling and global ocean
 886 state estimation. *Geoscientific Model Development*, *8*(10), 3071–3104.
- 887 Ghosh, D., & Baeder, J. D. (2012). High-order accurate incompressible Navier–Stokes
 888 algorithm for vortex-ring interactions with solid wall. *AIAA journal*, *50*(11), 2408–
 889 2422.
- 890 Godunov, S. K. (1959). A difference scheme for numerical solution of discontinuous solution
 891 of hydrodynamic equations. *Matematicheskii Sbornik*, *47*, 271–306. (Translated by US
 892 Joint Publications Research Service, JPRS 7226, 1969)
- 893 Grachev, A. A., Andreas, E. L., Fairall, C. W., Guest, P. S., & Persson, P. O. G. (2007). Sheba
 894 flux–profile relationships in the stable atmospheric boundary layer. *Boundary-layer*
 895 *meteorology*, *124*, 315–333.
- 896 Griffies, S. M., Adcroft, A., & Hallberg, R. W. (2020). A primer on the vertical lagrangian-
 897 remap method in ocean models based on finite volume generalized vertical coordinates.
 898 *Journal of Advances in Modeling Earth Systems*, *12*(10), e2019MS001954.
- 899 Griffies, S. M., Pacanowski, R. C., & Hallberg, R. W. (2000). Spurious diapycnal mixing
 900 associated with advection in a z-coordinate ocean model. *Monthly Weather Review*,
 901 *128*(3), 538–564.
- 902 Griffies, S. M., Stouffer, R. J., Adcroft, A. J., Bryan, K., Dixon, K. W., Hallberg, R., ...
 903 Rosati, A. (2015). A historical introduction to MOM. URL https://www.gfdl.noaa.gov/wp-content/uploads/2019/04/mom_history_2017, 9.
- 904 Häfner, D., Nuterman, R., & Jochum, M. (2021). Fast, cheap, and turbulent—global ocean
 905 modeling with GPU acceleration in Python. *Journal of Advances in Modeling Earth*
 906 *Systems*, *13*(12), e2021MS002717.
- 907 Halliwell, G. R. (2004). Evaluation of vertical coordinate and vertical mixing algorithms in
 908 the HYbrid-Coordinate Ocean Model (HYCOM). *Ocean Modelling*, *7*(3-4), 285–322.
- 909 Held, I. M. (2005). The gap between simulation and understanding in climate modeling.
 910 *Bulletin of the American Meteorological Society*, *86*(11), 1609–1614.
- 911 Huang, N. E. (1979). On surface drift currents in the ocean. *Journal of Fluid Mechanics*,
 912 *91*(1), 191–208.
- 913 Kärnä, T., Kramer, S. C., Mitchell, L., Ham, D. A., Piggott, M. D., & Baptista, A. M.
 914 (2018). Thetis coastal ocean model: discontinuous Galerkin discretization for the
 915 three-dimensional hydrostatic equations. *Geoscientific Model Development*, *11*(11),
 916 4359–4382.
- 917 Kiss, A. E., Hogg, A. M., Hannah, N., Boeira Dias, F., Brassington, G. B., Chamberlain,
 918 M. A., ... others (2020). Access-om2 v1. 0: a global ocean–sea ice model at three
 919 resolutions. *Geoscientific Model Development*, *13*(2), 401–442.
- 920 Klöwer, M., Gelbrecht, M., Hotta, D., Willmert, J., Silvestri, S., Wagner, G. L., ... others
 921 (2024). Speedyweather. jl: Reinventing atmospheric general circulation models towards
 922 interactivity and extensibility. *Journal of Open Source Software*, *9*(98), 6323.
- 923 Kochkov, D., Yuval, J., Langmore, I., Norgaard, P., Smith, J., Mooers, G., ... others
 924 (2024). Neural general circulation models for weather and climate. *Nature*, *632*(8027),
 925 1060–1066.
- 926 Korn, P., Brüggemann, N., Jungclaus, J. H., Lorenz, S., Gutjahr, O., Haak, H., ... others
 927 (2022). Icon-o: The ocean component of the icon earth system model—global simulation
 928 characteristics and local telescoping capability. *Journal of Advances in Modeling Earth*
 929 *Systems*, *14*(10), e2021MS002952.
- 930 Lam, R., Sanchez-Gonzalez, A., Willson, M., Wirnsberger, P., Fortunato, M., Alet, F., ...
 931 others (2023). Learning skillful medium-range global weather forecasting. *Science*,
 932 *382*(6677), 1416–1421.
- 933 Leclair, M., & Madec, G. (2011). z-coordinate, an arbitrary lagrangian–eulerian coordinate
 934 separating high and low frequency motions. *Ocean Modelling*, *37*(3-4), 139–152.
- 935

- 936 Lilly, D. K. (1983). Stratified turbulence and the mesoscale variability of the atmosphere.
937 *Journal of the Atmospheric Sciences*, *40*(3), 749–761.
- 938 Marshall, J., Adcroft, A., Hill, C., Perelman, L., & Heisey, C. (1997). A finite-volume,
939 incompressible Navier Stokes model for studies of the ocean on parallel computers.
940 *Journal of Geophysical Research: Oceans*, *102*(C3), 5753–5766.
- 941 Marshall, J., Hill, C., Perelman, L., & Adcroft, A. (1997). Hydrostatic, quasi-hydrostatic, and
942 nonhydrostatic ocean modeling. *Journal of Geophysical Research: Oceans*, *102*(C3),
943 5733–5752.
- 944 McDougall, T. J., & Barker, P. M. (2011). Getting started with TEOS-10 and the Gibbs
945 Seawater (GSW) oceanographic toolbox. *Scor/iapso WG*, *127*(532), 1–28.
- 946 Molemaker, M. J., McWilliams, J. C., & Capet, X. (2010). Balanced and unbalanced routes
947 to dissipation in an equilibrated eady flow. *Journal of Fluid Mechanics*, *654*, 35–63.
- 948 Monin, A. (n.d.). Basic laws of turbulent mixing in the surface layer of the atmosphere.
- 949 Moses, W. S., Churavy, V., Paehler, L., Hüchelheim, J., Narayanan, S. H. K., Schanen, M.,
950 & Doerfert, J. (2021). Reverse-mode automatic differentiation and optimization of gpu
951 kernels via enzyme. In *Proceedings of the international conference for high performance*
952 *computing, networking, storage and analysis* (pp. 1–16).
- 953 Murray, R. J. (1996). Explicit generation of orthogonal grids for ocean models. *Journal of*
954 *Computational Physics*, *126*(2), 251–273.
- 955 National Energy Research Scientific Computing Center. (2025). *Perlmutter archi-*
956 *tecture*. Retrieved from [https://docs.nersc.gov/systems/perlmutter/](https://docs.nersc.gov/systems/perlmutter/architecture/)
957 [architecture/](https://docs.nersc.gov/systems/perlmutter/architecture/) (Accessed: 2025-02-18)
- 958 Pawlak, G., MacCready, P., Edwards, K., & McCabe, R. (2003). Observations on the
959 evolution of tidal vorticity at a stratified deep water headland. *Geophysical Research*
960 *Letters*, *30*(24).
- 961 Pearson, B. (2018). Turbulence-induced anti-Stokes flow and the resulting limitations of
962 large-eddy simulation. *Journal of Physical Oceanography*, *48*(1), 117–122.
- 963 Petersen, M. R., Jacobsen, D. W., Ringler, T. D., Hecht, M. W., & Maltrud, M. E. (2015).
964 Evaluation of the arbitrary Lagrangian–Eulerian vertical coordinate method in the
965 MPAS-Ocean model. *Ocean Modelling*, *86*, 93–113.
- 966 Phillips, N. A. (1956). The general circulation of the atmosphere: A numerical experiment.
967 *Quarterly Journal of the Royal Meteorological Society*, *82*(352), 123–164.
- 968 Pressel, K. G., Kaul, C. M., Schneider, T., Tan, Z., & Mishra, S. (2015). Large-eddy
969 simulation in an anelastic framework with closed water and entropy balances. *Journal*
970 *of Advances in Modeling Earth Systems*, *7*(3), 1425–1456.
- 971 Pressel, K. G., Mishra, S., Schneider, T., Kaul, C. M., & Tan, Z. (2017). Numerics and
972 subgrid-scale modeling in large eddy simulations of stratocumulus clouds. *Journal of*
973 *Advances in Modeling Earth Systems*, *9*(2), 1342–1365.
- 974 Ramadhan, A., Wagner, G., Hill, C., Campin, J.-M., Churavy, V., Besard, T., ... Marshall,
975 J. (2020). Oceananigans.jl: Fast and friendly geophysical fluid dynamics on GPUs.
976 *Journal of Open Source Software*, *5*(53).
- 977 Ringler, T., Petersen, M., Higdon, R. L., Jacobsen, D., Jones, P. W., & Maltrud, M. (2013).
978 A multi-resolution approach to global ocean modeling. *Ocean Modelling*, *69*, 211–232.
- 979 Roquet, F., Madec, G., Brodeau, L., & Nycander, J. (2015). Defining a simplified yet
980 “realistic” equation of state for seawater. *Journal of Physical Oceanography*, *45*(10),
981 2564–2579.
- 982 Roquet, F., Madec, G., McDougall, T. J., & Barker, P. M. (2015). Accurate polynomial
983 expressions for the density and specific volume of seawater using the TEOS-10 standard.
984 *Ocean Modelling*, *90*, 29–43.
- 985 Rozema, W., Bae, H. J., Moin, P., & Verstappen, R. (2015). Minimum-dissipation models
986 for large-eddy simulation. *Physics of Fluids*, *27*(8).
- 987 Schumann, U., & Sweet, R. A. (1988). Fast Fourier transforms for direct solution of Poisson’s
988 equation with staggered boundary conditions. *Journal of Computational Physics*,
989 *75*(1), 123–137.
- 990 Shchepetkin, A. F., & McWilliams, J. C. (2005). The regional oceanic modeling system

- 991 (ROMS): a split-explicit, free-surface, topography-following-coordinate oceanic model.
 992 *Ocean modelling*, 9(4), 347–404.
- 993 Shu, C. (1997). *Essentially non-oscillatory and weighted essentially non-oscillatory schemes*
 994 *for hyperbolic conservation laws* (ICASE Report No. 97-65). Institute for Computer
 995 Applications in Science and Engineering, NASA Langley Research Center.
- 996 Shu, C.-W. (2009). High order weighted essentially nonoscillatory schemes for convection
 997 dominated problems. *SIAM review*, 51(1), 82–126.
- 998 Silvestri, S., Wagner, G. L., Campin, J.-M., Constantinou, N. C., Hill, C. N., Souza, A., &
 999 Ferrari, R. (2024). A new WENO-based momentum advection scheme for simulations
 1000 of ocean mesoscale turbulence. *Journal of Advances in Modeling Earth Systems*, 16(7),
 1001 e2023MS004130.
- 1002 Silvestri, S., Wagner, G. L., Constantinou, N. C., Hill, C. N., Campin, J.-M., Souza, A. N., ...
 1003 Ferrari, R. (2024). A GPU-based ocean dynamical core for routine mesoscale-resolving
 1004 climate simulations. *Authorea Preprints*. doi: 10.22541/essoar.171708158.82342448/v1
- 1005 Smagorinsky, J. (1963). General circulation experiments with the primitive equations: I.
 1006 The basic experiment. *Monthly weather review*, 91(3), 99–164.
- 1007 Stone, P. H. (1971). Baroclinic stability under non-hydrostatic conditions. *Journal of Fluid*
 1008 *Mechanics*, 45(4), 659–671.
- 1009 Strong-Wright, J., Chen, S., Constantinou, N. C., Silvestri, S., Wagner, G. L., & Taylor, J. R.
 1010 (2023). OceanBioME.jl: A flexible environment for modelling the coupled interactions
 1011 between ocean biogeochemistry and physics. *Journal of Open Source Software*, 8(90),
 1012 5669.
- 1013 Tsujino, H., Urakawa, S., Nakano, H., Small, R. J., Kim, W. M., Yeager, S. G., ... others
 1014 (2018). JRA-55 based surface dataset for driving ocean–sea-ice models (JRA55-do).
 1015 *Ocean Modelling*, 130, 79–139.
- 1016 Umlauf, L., & Burchard, H. (2003). A generic length-scale equation for geophysical turbulence
 1017 models.
- 1018 Umlauf, L., & Burchard, H. (2005). Second-order turbulence closure models for geophysical
 1019 boundary layers. a review of recent work. *Continental Shelf Research*, 25(7-8), 795–827.
- 1020 Vanneste, J., & Young, W. R. (2022). Stokes drift and its discontents. *Philosophical*
 1021 *Transactions of the Royal Society A*, 380(2225), 20210032.
- 1022 Vreugdenhil, C. A., & Taylor, J. R. (2018). Large-eddy simulations of stratified plane Couette
 1023 flow using the anisotropic minimum-dissipation model. *Physics of Fluids*, 30(8).
- 1024 Wagner, G. L., Chini, G. P., Ramadhan, A., Gallet, B., & Ferrari, R. (2021). Near-inertial
 1025 waves and turbulence driven by the growth of swell. *Journal of Physical Oceanography*,
 1026 51(5), 1337–1351.
- 1027 Wagner, G. L., Hillier, A., Constantinou, N. C., Silvestri, S., Souza, A. N., Burns, K., ...
 1028 others (2025). Formulation and calibration of CATKE, a one-equation parameterization
 1029 for microscale ocean mixing. *Authorea Preprints*. doi: 10.48550/arXiv.2306.13204
- 1030 Wagner, G. L., Silvestri, S., Constantinou, N. C., Strong-Wright, J., Byrne, S., Bozzola, G., ...
 1031 Churavy, V. (2025, February). *CliMA/ClimaOcean.jl: v0.4.0*. Zenodo. Retrieved from
 1032 <https://doi.org/10.5281/zenodo.14890032> doi: 10.5281/zenodo.14890032
- 1033 Warner, S. J., & MacCready, P. (2014). The dynamics of pressure and form drag on a sloping
 1034 headland: Internal waves versus eddies. *Journal of Geophysical Research: Oceans*,
 1035 119(3), 1554–1571.
- 1036 Watt-Meyer, O., Dresdner, G., McGibbon, J., Clark, S. K., Henn, B., Duncan, J., ... others
 1037 (2023). ACE: A fast, skillful learned global atmospheric model for climate prediction.
 1038 *arXiv preprint arXiv:2310.02074*.
- 1039 Watt-Meyer, O., Henn, B., McGibbon, J., Clark, S. K., Kwa, A., Perkins, W. A., ... Brether-
 1040 ton, C. S. (2024). ACE2: Accurately learning subseasonal to decadal atmospheric
 1041 variability and forced responses. *arXiv preprint arXiv:2411.11268*.
- 1042 Yatunin, D., Byrne, S., Kawczynski, C., Kandala, S., Bozzola, G., Sridhar, A., ... others
 1043 (2025). The Climate Modeling Alliance Atmosphere Dynamical Core: Concepts,
 1044 Numerics, and Scaling. *Authorea Preprints*.